Nonlinear Optical Noise Measurements with Atomic Force Microscopy

Adam J. Czarnecki, Department of Physics

McGill University, Montreal

December 2024

A thesis submitted to McGill University in partial fulfillment of the requirements of the degree of Master of Science.

Abstract

The nonlinear optical response of materials is of great interest for optoelectronic applications. In particular, it is important to be able to spatially resolve variations in the nonlinear properties of a material. This can be achieved by ultrafast atomic force microscopy (AFM), though there are spatial resolution limitations to previous implementations of this experimental technique as the measurement takes a long time. This work aims to show improvements to measuring nonlinear optical properties with ultrafast AFM using noise measurements. Such measurements allow for a faster characterization of the nonlinear properties with better spatial resolution.

Resumé

La réponse optique non linéaire des matériaux présente un grand intérêt pour les applications optoélectroniques. En particulier, il est important de pouvoir résoudre spatialement les variations des propriétés non linéaires d'un matériel. Ceci peut être réalisé par microscopie à force atomique (AFM) ultrarapide. Cependant, les mises en œuvre précédentes de cette technique expérimentale présentent des limites en termes de résolution spatiale, car la mesure prend beaucoup de temps. Ce travail vise à montrer les améliorations apportées à la mesure des propriétés optiques non linéaires avec l'AFM ultrarapide grâce à l'utilisation de mesures de bruit. De telles mesures permettent une caractérisation plus rapide des propriétés non linéaires avec une meilleure résolution spatiale.

Acknowledgments

Thank you to my supervisor Peter for your support and mentorship throughout my studies. I am especially grateful for your generosity with the time you gave me in lengthy scientific discussions as well as figuring out my experiments in the lab.

I would also like to thank Dave for lending his ear when I had questions about my work, and for generously sharing his lab resources. I am also very grateful that you agreed to be the external reviewer of this thesis.

Thank you to Professor Klaus Meerholz's group who supplied the HB238 sample, and to Dr. Kuan Eng Johnson Goh's group who supplied the WS_2 sample. These samples were critical in this work.

Thank you to the Grütter group, especially the Wong subgroup members over the last two years who supported me in my work: Simon, Wyatt, Megan, and Josephine. Thank you to Megan and Josephine for teaching me how to run the JEOL system. Thank you Catherine for helping me navigate confusing bureaucracies and also helping with the French version of my abstract. Thank you also to the other group members: José, Nata, Sean C, Sean M, Lily, and Yacine. I'm also very grateful for the members of the Cooke group that helped me figure out all my optics problems, especially Rodrigo and Ben C. Finally, I'd like to thank Robert Idsinga and Robert Turner for your help in figuring out technical problems in my experiments.

I would also like to thank the many wonderful people I have met outside of my studies during my time at McGill. Thank you to all at the Newman Centre of McGill and the

Newman Catholic Students' Society, especially Fr. Anthony, for helping me remember what is truly the most important. Thank you also to the McGill Rowing team, especially the coaches: Phil, Steph, Gijs, and James. You have taught me many things about resilience, patience, teamwork, and leadership.

Finally, thank you to my friends and family for your endless love and support throughout my journey. I could not have done this without you.

Contribution of Authors

Chapter 1 and the first half of chapter 2 are a review of background knowledge. This includes an overview of work done by previous students, notably Zeno Schumacher and Rasa Rejali. The second half of chapter 2 discusses data analysis methods developed by the author. Chapter 3 presents an overview of the experimental setup, which was largely adapted from the setup developed by Zeno Schumacher and Rasa Rejali. The characterization of the experimental setup in chapter 3 was done by the author. Chapters 4 and 5 present measurements done by the author.

Contents

1 Introduction **1**

1.1 Scanning Probe Microscopy 1

1.2 Ultrafast STM and AFM 3

1.3 Measuring Nonlinear Optics with Ultrafast AFM 4

2 Background **6**

2.1 Atomic Force Microscopy 6

2.2 Second-Order Polarization $P^{(2)}$ and Susceptibility $\chi^{(2)}$ 8

2.3 Autocorrelation of Ultrafast Laser Pulses 11

2.4 Measuring Optical Nonlinearity with Ultrafast AFM 13

2.5 Extracting the Autocorrelation Amplitude 16

2.5.1 Gaussian Fitting 16

2.5.2 Sine Fitting 18

2.6 Noise Analysis 19

2.7 Samples Investigated 21

3 Experimental Methods **24**

3.1 The AFM System 24

3.2 Optical System 25

3.2.1 Beam Alignment 27

3.2.2 Polarization Rotation in Periscope 31

3.3 Ultrafast AFM 32
3.3.1 Verifying Nonlinear Optical Effects 34
3.3.2 Measuring Nonlinear Optics with Noise 35

4 Ultrafast AFM Measurements 38

4.1 Monolayer WS_2 on Sapphire Substrate 38
4.1.1 Autocorrelation Amplitude vs Tip Height 40
4.1.2 Autocorrelation Amplitude and Noise vs Laser Power 41
4.1.3 Spatial Measurement 43

5 Conclusion and Outlook 46

Bibliography 49

List of Figures

2.1 An ideal autocorrelation of a 780 nm 100 fs gaussian pulse. 12
2.2 AFM autocorrelations on PPLN and on monolayer $MoSe_2$. 15
2.3 Gaussian envelope fit to a model autocorrelation signal. 17
2.4 Sine fitted to model autocorrelation. 19
2.5 σ-intensity trends. 20
2.6 Modelled noise distributions. 22
2.7 HB238 UV-vis spectra. 23

3.1 Experimental setup schematic. 26
3.2 Effect of uneven beam intensities on interferometric autocorrelation ratio. . . 28
3.3 Normalized interferometric autocorrelations with one and two bandpass filters. 30
3.4 The effect of a periscope on laser beam polarization. 31
3.5 Approached and retracted autocorrelation measurements. 33
3.6 AFM autocorrelation measurements with varying laser intensity. 36
3.7 Residual distribution of a sine fit to an autocorrelation measurement. 37

4.1 KPFM scan of a WS flake on a sapphire substrate. 39
4.2 z spectra of autocorrelation amplitude and noise over WS_2 and sapphire. . . 41
4.3 Intensity measurements on WS_2 and sapphire. 42
4.4 A line measurement on WS_2 and sapphire. 45

5.1 Dissipation scan of a SiO_2 surface with a 3 nm oxide overgrowth. 48

Nomenclature

2D TMD	2-dimensional transition metal dichalcogenide
AFM	Atomic force microscopy
AM	Amplitude modulated
BBO	Beta barium borate
CPD	Contact potential difference
CVD	Chemical vapour deposition
DFG	Difference frequency generation
DOS	Density of states
FM	Frequency modulated
HHG	Half harmonic generation
KPFM	Kelvin probe force microscopy
OR	Optical rectification
PIFM	Photo induced force microscopy
PLL	Phase-lock loop
PPLN	Periodically poled lithium niobate
PSD	Power spectral density
SFG	Sum frequency generation
SHG	Second harmonic generation
SPM	Scanning probe microscopy
STM	Scanning tunneling microscopy
UHV	Ultra-high vacuum
UV-Vis	Ultraviolet-visible

Chapter 1

Introduction

1.1 Scanning Probe Microscopy

Since the invention of the transistor in the 1950's, technology miniaturization has exploded in popularity, sparking the development of the field of nanotechnology. Developing smaller scale electronics, especially transistors, allows for the production of more dense electronic circuits with lower energy consumption and high computational power. An important field that was important in the development of nanotechnology was that of material science, especially surface science, as being able to accurately control the growth of materials is necessary in the production of nanoscale electronics. While the method of growing pure crystals was already well established with the Czochralski method [1], deposition of additional materials on a clean crystal surface was conducted to build nanoscale systems. Imaging these systems was routinely done by the well established electron microscope [2, 3]. However, the electron microscope was not able to image surfaces at the atomic scale, which eventually was deemed necessary to understand the precise structure of surfaces, such as 7×7 surface reconstruction of Si(111).

The scanning tunneling microscope (STM) was invented in the early 1981 by Binnig and Rohrer, making atomic resolution imaging possible and paving the road to atomic-scale surface science [4]. STM relies on placing an ultra-sharp tip close to the sample surface to induce a tunneling current, and being able to move the tip very precisely. The technology needed to make the STM was known for quite a while before it was finally put together in the 1980's. The tunneling effect was already known in the 1920's, first being applied in understanding the theory of molecular spectra [5]. Piezoelectric mechanics, which are used for moving the STM tip, were experimentally confirmed by the Curie brothers in the 1880's [6]. The control systems needed, a function generator and feedback control, were also well understood in the early 20th century due to the development of aircraft and other technologies needed for World War 1 [7]. The closest anyone got to inventing the STM (before the actual invention) was in 1972, with the invention of the topografiner [8]. Even at that time the inventors of the topografiner noted that higher resolution could be achieved if it used the tunneling effect to image the surface.

Measuring the tunneling current over the surface can give much more insight into the physics of the sample than just the topography of the surface. Scanning the tip across the surface can also map out the density of states (DOS) of the sample's surface, giving insight into the electronic nature of the surface. However, given that this method relies on tunneling current, it does not work with insulating samples and is limited to metal and semiconductor samples. To conquer this problem, atomic force microscopy (AFM) was invented as an alternative method that could study insulating materials as well [9].

AFM works on the principle of detecting forces in close proximity to the sample surface. These forces include short range (a few nm) chemical forces and long range (∼100 nm) van der Waals, electrostatic, and magnetic forces [10]. The AFM probe is also sharp like the STM probe, but is instead mounted on a flexible cantilever. In the early days of AFM, the cantilever was kept static and was only subject to deflections due to the surface forces. The challenge with the static mode operation was that the cantilever could easily be excited into an oscillation mode (for example, due to thermal excitation), and introduced significant noise to the measurement. To tackle this, dynamic AFM was developed where the cantilever was intentionally driven near the fundamental frequency f_0. Dynamic AFM can be performed via two basic methods: amplitude modulated (AM) and frequency modulated (FM) AFM. In AM-AFM, the cantilever is driven at a constant amplitude A_{drive} and frequency f_{drive} close to f_0 [11]. Forces acting on the tip lead to a change in the cantilever amplitude, which can be used as an imaging signal, as well as a feedback signal to keep A_{drive} constant. In FM-AFM, changes in the oscillation frequency are instead used as an imaging and feedback signal [12].

1.2 Ultrafast STM and AFM

The invention of ultrafast pulsed lasers was an important development that allowed for measuring ultrafast events. The 1999 Nobel Prize in chemistry was awarded to Ahmed Zewail for application of ultrafast pulses to study chemical reactions at the femtosecond scale [13, 14]. The coupling of ultrafast lasers with scanning probe microscopy (SPM) allows for the observation of temporal events in a material, as well as other optical and electronic properties, with spatial resolution. This forms the field of ultrafast SPM.

There have been many different ways of creating ultrafast SPM with various applications. Carrier life times in materials are typically studied with pump-probe experiments, where a “pump” pulse excites carriers in the material, and a “probe” pulse is used to study the changes in the material at various time intervals after the initial excitation by the pump. Pump-probe experiments have been done by STM [15, 16, 17] and AFM [18, 19]. There are other properties other than carrier dynamics that can be studied with such ultrafast SPM setups. For example, one can measure photovoltaic properties of a material [20] or molecular resonances induced by pulsed illumination [21].

1.3 Measuring Nonlinear Optics with Ultrafast AFM

The material property that is of interest in this work is the second-order electric susceptibility $\chi^{(2)}$. It has been found that materials with nonzero $\chi^{(2)}$ can be used for half harmonic generation (HHG), in which the material produces two entangled photons with frequency $\omega/2$ for every absorbed photon of frequency ω, as well as for second harmonic generation (SHG), in which the material combines two photons of frequency ω to produce one photon of frequency 2ω [22, 23]. Such properties would be beneficial for quantum device applications where entangled photons are needed [24].

Nonlinear optical properties were first measured by ultrafast AFM by Jahng *et al*. [18]. This ultrafast AFM technique is known as photo induced force microscopy (PIFM), and it detects the induced dipoles in the tip and sample. The challenge with this technique is that it is limited to detecting forces in the near field. A development to measuring nonlinear optical properties with ultrafast AFM was demonstrated by Schumacher *et al*. [25]. In this method, laser pulse pairs are directed onto the sample to induce a polarization that can be detected by the AFM. By controlling the time delay between subsequent laser pulses, one can perform an interferometric autocorrelation and characterize $\chi^{(2)}$ of the sample surface, as $\chi^{(2)}$ is proportional to the amplitude of the interferometric autocorrelation signal. The details of this measurement will be discussed in chapter 3.

The challenge with this method is that performing interferometric autocorrelations is a slow process, often on the order of minutes This limits the spatial resolution one can achieve in a single image. For example, if one autocorrelation took 5 minutes at a single point on the sample, it would take about 2 weeks of continuous measurements to create a measly 64×64 pixel $\chi^{(2)}$ map. This is rather poor resolution compared to the standard 512×512 or 1024×1024 pixel images made with AFM.

It has been observed by Spiegelberg [26] that the noise in the AFM measurement depends on the intensity of the induced polarization, which changes with light intensity during the autocorrelation. As mentioned above, $\chi^{(2)}$ is proportional to the amplitude of the autocorrelation, and hence also to the noise amplitude. This provides a new way to characterize $\chi^{(2)}$. Since it is much faster to perform a noise measurement (on the order of seconds) than an autocorrelation (on the order of minutes), one could characterize $\chi^{(2)}$ with higher spatial resolution in less time, allowing for the correlation of nonlinear optical properties of surface defects to their structure.

This work aims to demonstrate how one can characterize $\chi^{(2)}$ spatially via noise measurements with ultrafast AFM. Chapter 2 will begin by explaining the scientific foundation of this project, such as how AFM and interferometric autocorrelation measurements work, as well as how AFM can measure the nonlinear polarization induced in the sample by ultrafast pulses. In chapter 3, details of the experimental setups of the optics table and the AFM, and how they are coupled together, will be discussed. In chapter 4, noise measurements that are conducted with this experimental setup will be shown.

Chapter 2

Background

The work conducted in this thesis is based on several different experimental techniques, mostly involving the combination of atomic force microscopy (AFM) and ultrafast optical experiments. This chapter aims to provide a theoretical overview of these techniques, starting with the fundamentals of AFM and nonlinear optics, and then describing how these can be combined to form the technique of ultrafast AFM and how it can be used to measure nonlinear optical properties of materials with spatial resolution. Data analysis methods used to analyze the ultrafast AFM signal will also be discussed.

2.1 Atomic Force Microscopy

Atomic force microscopy (AFM) is a type of scanning probe microscopy (SPM) that uses a sharp tip placed on the end of a flexible cantilever to measure interactions between the tip and the sample [9]. A detector is used to measure the deflection of the cantilever, which can be used to determine the force exerted on the tip by the sample. By raster scanning the surface, one can map out features of the sample.

To improve the signal to noise ratio, one can conduct frequency modulated AFM (FM-AFM) where the cantilever oscillates and the changes in the cantilever frequency are detected rather than the changes of the cantilever amplitude (as in amplitude modulated AFM) or static deflection [12]. To understand the dynamics of the cantilever, one can assume that the tip of mass m is mounted on the end of the massless cantilever and treat it as a damped-driven harmonic oscillator. The dynamics of such a system are described by the equation

$$m\ddot{z} + \frac{m\omega_0}{Q}\dot{z} + kz = F_{\mathrm{d}} \cos\left(\omega_{\mathrm{d}} t\right) + F_{\mathrm{ts}}\left(z\right), \tag{2.1}$$

where z is the tip-sample separation, $\omega_0 = \sqrt{\frac{k}{m}}$ is the resonant frequency of the cantilever, Q is the quality factor, k is the spring constant of the cantilever, F_{d} is the amplitude of the applied driving force, ω_{d} is the driving frequency, and F_{ts} is the tip-sample interaction force. The cantilever is first calibrated at a distance far from the sample where $F_{\mathrm{ts}} \approx 0$, allowing for ω_0 and Q to be determined by sweeping through a range of driving frequencies ω_{d} and finding the resonant frequency ω_0 where the oscillation amplitude is the largest.

Once ω_0 is known, the tip is approached to the sample until the frequency shift reaches the frequency shift setpoint $\Delta\omega$. A feedback loop (usually a phase-lock loop (PLL)) is used to maintain the setpoint $\Delta\omega$ by adjusting the tip height above the sample.

To relate F_{ts} to $\Delta\omega$, one can analyze equation 2.1. Since the driving force is used to compensate any damping the cantilever might experience (given by the $\dot{z}$ term in equation 2.1), we can equate the damping and driving terms [27]. Making this simplification, and using $m = \frac{k}{\omega_0^2}$, equation 2.1 becomes:

$$\frac{k}{\omega_0^2}\ddot{z} + kz = F_{\mathrm{ts}}\left(z\right). \tag{2.2}$$

One may rewrite $F_{\mathrm{ts}}(z)$ as a Taylor series about the equilibrium tip-sample separation z_0:

$$F_{\mathrm{ts}}(z) = F_{\mathrm{ts}}\left(z_0\right) + \frac{dF_{\mathrm{ts}}\left(z_0\right)}{dz}\left(z - z_0\right) + \ldots. \tag{2.3}$$

At small oscillation amplitudes, the first two terms of the series are sufficient to approximate $F_{\mathrm{ts}}(z)$. Substituting this into equation 2.2, and defining the effective spring constant $k_{\mathrm{eff}} =$

$k - dF_{\text{ts}}(z_0)/dz$:

$$\frac{k}{\omega_0^2}\ddot{z} + k_{\text{eff}} z = F_{\text{ts}}\left(z_0\right) - \frac{dF_{\text{ts}}\left(z_0\right)}{dz} z_0. \tag{2.4}$$

This new effective spring constant k_{eff} results in a new resonant frequency $\omega_{\text{eff}} = \sqrt{k_{\text{eff}}/m}$. The change in angular frequency, $\Delta\omega = \omega_{\text{eff}} - \omega_0$, may thus be expressed as

$$\Delta\omega = \sqrt{\frac{k}{m}}\left[\sqrt{1 - \frac{1}{k}\frac{dF_{\text{ts}}}{dz}} - 1\right] \approx -\frac{\omega_0}{2k}\frac{dF_{\text{ts}}\left(z_0\right)}{dz}, \tag{2.5}$$

where it was assumed that $dF_{\text{ts}}/dz \ll k$. Equation 2.5 indicates that the z-feedback loop that maintains a constant $\Delta\omega$ is adjusting the tip height z to maintain a constant tip-sample force gradient $dF_{\text{ts}}(z_0)/dz$.

The essence of FM-AFM is now established. The following sections will introduce some fundamentals of nonlinear optics, and how FM-AFM can be used to characterize nonlinear optical effects that take place in the sample.

2.2 Second-Order Polarization $P^{(2)}$ and Susceptibility $\chi^{(2)}$

This thesis discusses how AFM can be used to characterize nonlinear optical effects in a sample, in particular second-order optical effects. When making these characterizations, the AFM measures parts of the second-order polarization $P^{(2)}$. This section will introduce some fundamentals of nonlinear optics and explain what $P^{(2)}$ is, largely following the discussion presented in chapter 1 of Boyd's Nonlinear Optics [23].

In linear optics, when a material is placed in an electric field E, the induced polarization P in the material is given by

$$P(t) = \epsilon_0 \chi^{(1)} E(t), \tag{2.6}$$

where ϵ_0 is the permittivity of free space and $\chi^{(1)}$ is the linear electric susceptibility of the material [28]. For simplicity, we are considering P and E to be scalars. When $E(t)$ becomes sufficiently large, such as that of a laser, new phenomena take place within the material that lead to nonlinear contributions to the induced polarization $P(t)$. This is the regime of nonlinear optics, where $P(t)$ may be written as a power series in $E(t)$:

$$P(t) = \epsilon_0 \left(\chi^{(1)} E(t) + \chi^{(2)} E(t)^2 + \chi^{(3)} E(t)^3 + \ldots \right), \tag{2.7}$$

where $\chi^{(2,3)}$are the second and third order optical susceptibilities. One can write $P(t)$ as a sum of polarizations that correspond to each term in equation 2.7:

$$P(t) = P^{(1)}(t) + P^{(2)}(t) + P^{(3)}(t) + \ldots, \tag{2.8}$$

where the second-order polarization is

$$P^{(2)}(t) = \epsilon_0 \chi^{(2)} E(t)^2. \tag{2.9}$$

Suppose the electric field is that of a laser pulse, given by

$$\tilde{E}(t) = E(t) e^{-i\omega t} + \text{c.c.}, \tag{2.10}$$

where c.c. is the complex conjugate part of the previous terms, in this case $E^*(t)e^{i\omega t}$, $E(t)$ is the temporal profile of the beam (such as a pulse), and ω is the carrier frequency of the beam. If this beam is incident on a nonlinear optical material, then the induced $P^{(2)}(t)$ will be

$$P^{(2)}(t) = 2\epsilon_0 \chi^{(2)} E(t) E(t)^* + \left(\epsilon_0 \chi^{(2)} E(t)^2 e^{-i2\omega t} + \text{c.c.} \right). \tag{2.11}$$

The first term of $P^{(2)}(t)$ in equation 2.11 has a zero frequency term and forms the process known as optical rectification (OR). The second term has a frequency of 2ω and leads to second-harmonic generation (SHG), which is the process of generating radiation of frequency

2ω.

It will be shown later in this work that the polarization is induced by a pair of laser pulses. In the case of two laser pulses delayed by time τ, with electric fields $\tilde{E}(t)$ and $\tilde{E}(t+\tau)$, the resulting second-order polarization $P^{(2)}(t,\tau)$ is given by

$$P^{(2)}(t,\tau) = 2\epsilon_0\chi^{(2)}\left(|E(t)|^2 + |E(t+\tau)|^2\right) \quad \text{(OR)} \tag{2.12}$$

$$+ \epsilon_0\chi^{(2)}[E(t)^2 e^{-2i\omega_0 t} + E(t+\tau)^2 e^{-2i\omega_0 t} \quad \text{(SHG)} \tag{2.13}$$

$$+ 2E(t)E(t+\tau)e^{-2i\omega_0 t}e^{-i\omega_0\tau} \quad \text{(SFG)} \tag{2.14}$$

$$+ 2E(t)E^*(t+\tau)e^{i\omega_0\tau} + \text{c.c.}] \quad \text{(DFG)}, \tag{2.15}$$

where OR is optical rectification, SHG is second harmonic generation, SFG is sum frequency generation, and DFG is difference frequency generation.

Materials must have a non-centrosymmetric crystal structure to have a non-zero $\chi^{(2)}$ [23, 29]. A non-centrosymmetric crystal structure is one that has no central point about which the crystal pattern is symmetric. There may be an axis in the crystal structure that has the greatest asymmetric potential. If using linearly polarized light to induce $P^{(2)}$ in the material, it is best to align the light polarization along this axis to maximize the induced $P^{(2)}$. It is also important to direct the light along an optimal crystal axis through a process called phase matching [30]. Phase matching is important as the index of refraction may vary with the wavelength of light. This is important if one wants to optimize the second order process such as SHG. In such a case, phase matching ensures that newly generated second harmonic light will constructively interfere with the already existing second harmonic, thus optimizing the output. Fortunately, the case of detecting second order processes at a surface with AFM avoids these challenges. All surfaces have a broken symmetry and thus have a non-zero $\chi^{(2)}$ and exhibit second order processes. Additionally, the phase matching condition only becomes important when the light is propagating over larger distances (on the order of several wavelengths). The probe area of the AFM is much smaller than this so one does not need to worry about phase matching to detect second order processes with AFM. The specifics of AFM detection of second order effects will be discussed in section 2.4.

Now we understand the nature of the components of the second-order polarization $P^{(2)}(t)$. This will be necessary when discussing what can and cannot be detected with the experimental setup used in this work.

2.3 Autocorrelation of Ultrafast Laser Pulses

A big part of this work is measuring $\chi^{(2)}$ by performing an interferometric autocorrelation measurement of an ultrafast laser pulse. In this section I will begin by discussing the nature of ultrafast pulses and what is an autocorrelation. I will then show how a SHG crystal can be used in an autocorrelation to perform an interferometric autocorrelation and characterize the $\chi^{(2)}$ of the SHG crystal. A large part of the discussion of ultrafast pulses and autocorrelations presented here follows that of chapter 17 of Hooker and Webb's Laser Physics [31].

An ultrafast pulse is typically considered to be a pulse of electromagnetic radiation that has a duration of less than a picosecond. The electric field of an ultrafast pulse is given by

$$\tilde{E}(t) = E(t)e^{-i\omega_0 t} + \text{c.c.} = g(t)e^{i\phi(t)}e^{-i\omega_0 t} + \text{c.c.}, \tag{2.16}$$

where $E(t)$ describes the envelope of the laser pulse, ω_0 is the carrier frequency of the pulse, $g(t) = |E(t)|$, and $\phi(t) = \arg(E(t))$ is the phase of the field amplitude [31]. Figure 2.1a shows the electric field of a 100 fs ultrafast pulse with a gaussian envelope and a carrier frequency corresponding to 780 nm light.

An autocorrelation measurement measures the intensity of two overlapped ultrafast laser pulses as a function of the delay time τ between the pulses. In practice, this is done by sending one pulse into an interferometer and varying τ by varying the position of one of the mirrors in the interferometer. The intensity $I_F(\tau)$ of the pulses delayed by τ is measured by

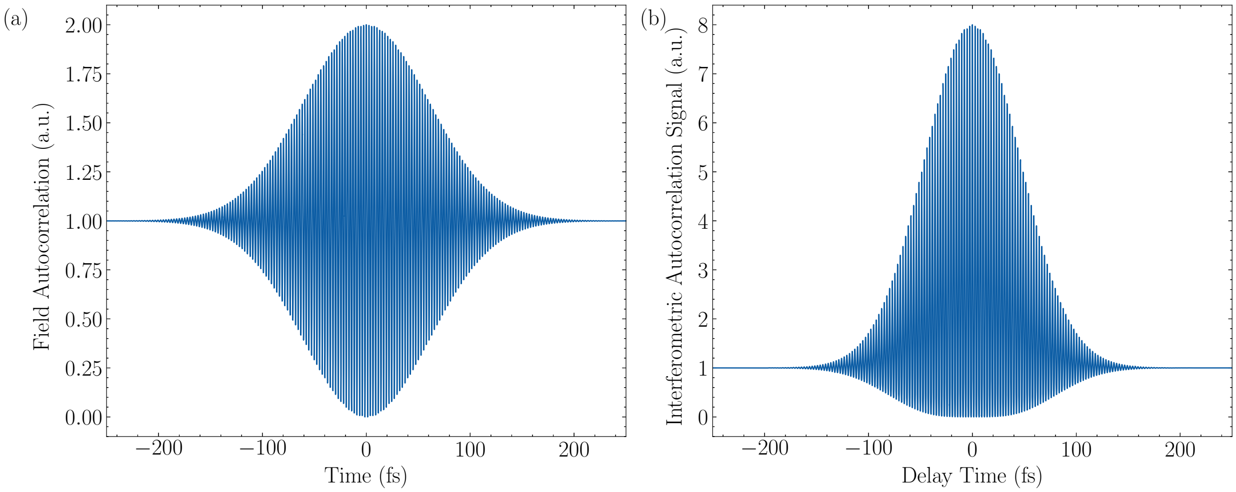

Figure 2.1: An ideal autocorrelation of a 780 nm 100 fs gaussian pulse. **(a)** A field autocorrelation of the laser pulse. **(b)** An interferometric autocorrelation of the laser pulse.

a photodetector, and is given by

$$I_F(\tau) = \int_{-\infty}^{\infty} |E(t) + E(t+\tau)|^2 \, dt. \tag{2.17}$$

This is known as the field autocorrelation, and a theoretical example is shown in figure 2.1a.

One can also pass the pulses through a SHG crystal to perform an interferometric autocorrelation. When the pulses are subsequently passed through a filter to only select the second harmonic light, the signal $S(\tau)$ measured by the photodetector is given by

$$S(\tau) \propto \int_{-\infty}^{\infty} \left(|E(t) + E(t+\tau)|^2\right)^2 dt. \tag{2.18}$$

The interferometric autocorrelation is plotted in figure 2.1b.

One can rewrite the interferometric autocorrelation signal in terms of light intensities using equation 2.16 by substituting

$$|E(t) + E(t+\tau)|^2 = I(t) + I(t+\tau) + 2\sqrt{I(t)I(t+\tau)}\cos\left(\omega_0\tau - \delta\phi\right), \tag{2.19}$$

where the first two terms are the intensities due to the individual pulses, and the third term describes the interference and $\delta\phi = \phi(t+\tau) - \phi(t)$ being the phase difference of the pulses. Substituting this into equation 2.18:

$$\begin{aligned} S(\tau) \propto & \int_{-\infty}^{\infty} I(t)^2 + 2I(t)I(t+\tau)dt && (2.20) \\ & + \int_{-\infty}^{\infty} I(t)I(t+\tau)\cos\left[2\left(\omega_0\tau - \delta\phi\right)\right]dt && (2.21) \\ & + 2\int_{-\infty}^{\infty} \left(I(t) + I(t+\tau)\right)\sqrt{I(t)I(t+\tau)}\cos\left(\omega_0\tau - \delta\phi\right)dt. && (2.22) \end{aligned}$$

Comparing the amplitude of the signal at the peak of the interferometric autocorrelation at $\tau = 0$ to the signal at no overlap at $\tau \to \infty$, we find that

$$\frac{S(\tau=0)}{S(\tau\to\infty)} = \frac{8\int_{-\infty}^{\infty} I(t)^2 dt}{\int_{-\infty}^{\infty} I(t)^2 dt} = 8, \tag{2.23}$$

which explains the well known 8:1 amplitude ratio observed in interferometric autocorrelations, seen in figure 2.1b.

2.4 Measuring Optical Nonlinearity with Ultrafast AFM

Here we will consider what the AFM detects when a pair of pulses induce a polarization in the sample. This discussion is inspired by that presented in 1.2.2 of [23], as well as [25]. Recall from section 2.2 that the second-order polarization $P^{(2)}$ induced by a pair of pulses delayed by time τ is given by

$$\begin{aligned} P^{(2)}(t,\tau) = & 2\epsilon_0\chi^{(2)}\left(|E(t)|^2 + |E(t+\tau)|^2\right) \quad \text{(OR)} && (2.24) \\ & + \epsilon_0\chi^{(2)}[E(t)^2 e^{-2i\omega_0 t} + E(t+\tau)^2 e^{-2i\omega_0 t} \quad \text{(SHG)} && (2.25) \\ & + 2E(t)E(t+\tau)e^{-2i\omega_0 t}e^{-i\omega_0\tau} \quad \text{(SFG)} && (2.26) \\ & + 2E(t)E^*(t+\tau)e^{i\omega_0\tau} + \text{c.c.}] \quad \text{(DFG)}. && (2.27) \end{aligned}$$

The driving angular frequency ω_d of the cantilever (with a frequency on the order of several hundred kilohertz) is much smaller than the carrier angular frequency ω_0 of the ultrafast pulses (with a frequency on the order of several hundred terahertz). Hence only the OR and DFG terms of $P^{(2)}(t,\tau)$, given in equations 2.24 and 2.27, can be detected by AFM. This is because the OR has no oscillations and the DFG term only oscillates as τ is varied. The SHG and SFG terms oscillate with frequency $2\omega_0$, which cannot be detected by the much slower cantilever. The OR term of $P^{(2)}(t,\tau)$, denoted by $P^{(2)}_{\mathrm{OR}}(t)$, manifests itself as a constant offset in the autocorrelation signal, while the DFG term, denoted by $P^{(2)}_{\mathrm{DFG}}(t,\tau)$, oscillates as τ is varied.

The electric potentials induced by the polarizations $P^{(2)}_{\mathrm{OR}}(t)$ and $P^{(2)}_{\mathrm{DFG}}(t,\tau)$ are denoted by $\phi_{\mathrm{OR}}(t)$ and $\phi_{\mathrm{DFG}}(t,\tau)$, respectively. These can be added into a common potential $\phi_{\mathrm{pol}}(t,\tau) = \phi_{\mathrm{OR}}(t) + \phi_{\mathrm{DFG}}(t,\tau)$ arising from the induced polarization. The resulting electrostatic force that the AFM detects is given by

$$F_{\mathrm{elec}}(t,\tau) = \frac{1}{2}\frac{dC}{dz}\left(V_{\mathrm{CPD}} - V_{\mathrm{DC}} - \phi_{\mathrm{pol}}(t,\tau)\right)^2, \tag{2.28}$$

with C being the tip-sample capacitance, z the tip-sample distance, V_{CPD} the contact potential difference between the tip and the sample, and V_{DC} the applied bias to the tip [32, 33]. One should note that [25] uses ϕ_{pol} to denote the electric potential energy rather than the electric potential, and thus includes an extra factor of $1/e$ in the last term of equation 2.28, with e being the elementary charge. Since $\phi_{\mathrm{OR}}(t)$ manifests itself as a constant offset, equation 2.28 may be rewritten as

$$F_{\mathrm{elec}}(t,\tau) = \frac{1}{2}\frac{dC}{dz}\left(V_{\mathrm{BG}} - \phi_{\mathrm{DFG}}(t,\tau)\right)^2, \tag{2.29}$$

where $V_{\mathrm{BG}} = V_{\mathrm{CPD}} - V_{\mathrm{DC}} - \phi_{\mathrm{OR}}(t)$ is the electrostatic background.

In frequency modulated AFM (FM-AFM), which was discussed in section 2.1, the frequency shift $\Delta f \propto dF/dz$ is detected. So the FM-AFM signal measured when probing the electrostatic force given by equation 2.29 is

$$\Delta f \propto \left(V_{\mathrm{BG}} - \phi_{\mathrm{DFG}}(t,\tau)\right)^2 . \tag{2.30}$$

Since $\phi_{\mathrm{DFG}}(t,\tau) \propto P^{(2)}_{\mathrm{DFG}}(t,\tau) \propto \chi^{(2)}$ (using equation 2.15), the magnitude of the oscillations of the Δf signal as τ is varied is proportional to $\chi^{(2)2}$. Also, the magnitude of the oscillations of Δf has a quadratic dependence on the intensity of the laser. One should note that the shape of the autocorrelation measured with FM-AFM depends on the relative magnitudes between V_{BG} and ϕ_{DFG}, and will often result in a different shape than that presented in figure 2.1b, which would be measured by a photodiode. An example of how variations in the relative magnitudes between V_{BG} and ϕ_{DFG} can affect the symmetry of AFM autocorrelations is shown in figure 2.2. These autocorrelation measurements were conducted on periodically poled lithium niobate (PPLN) and on monolayer $\mathrm{MoSe_2}$, and were plotted using data from [25].

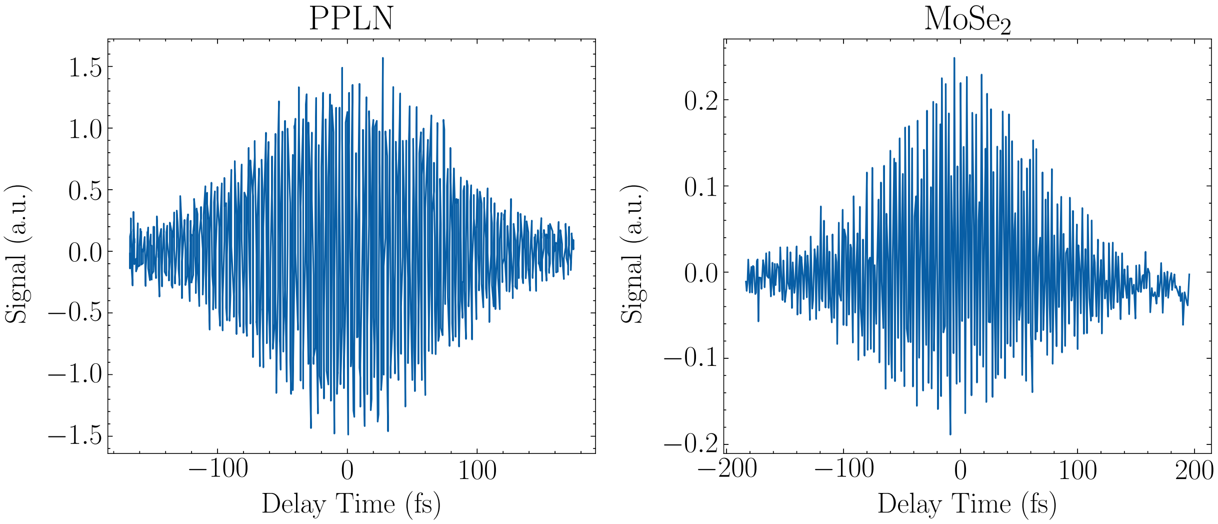

Figure 2.2: AFM autocorrelations on PPLN (left) and on monolayer $\mathrm{MoSe_2}$ (right). The autocorrelation on PPLN has a symmetric shape about the baseline while on $\mathrm{MoSe_2}$ it is asymmetric. This is caused by variations in the relative strengths of V_{BG} and ϕ_{DFG} in equation 2.30. This figure was generated using data from [25].

It is also worth considering the effects of the polarization terms beyond the second-order term shown in equation 2.7. Let us consider for example the third-order polarization $P^{(3)}$

induced by a pair of ultrafast pulses $\tilde{E}_1$ and $\tilde{E}_2$, each with carrier frequency ω_0:

$$P^{(3)}(t,\tau) = \varepsilon_0 \chi^{(3)} \left(\tilde{E}_1 + \tilde{E}_2\right)^3 = \varepsilon_0 \chi^{(3)} \left(\tilde{E}_1^3 + \tilde{E}_2^3 + 3\tilde{E}_1\tilde{E}_2^2 + 3\tilde{E}_1^2\tilde{E}_2\right). \tag{2.31}$$

Each of these terms oscillates with frequency $2\omega_0$ or $3\omega_0$, and thus cannot be detected by AFM. Expanding this consideration to further order terms, one sees that only even ordered polarization terms will have static and quasi-static (only oscillates with τ) that can be detected by AFM, while odd ordered terms will not have these terms and are not detectable by AFM.

2.5 Extracting the Autocorrelation Amplitude

The information that this work is interested in extracting from an autocorrelation measurement is the amplitude at the zero time delay in order to characterize the magnitude of $\chi^{(2)}$ at the location of the measurement. There are two main methods that have been used in this work. The first method applies to extracting the amplitude from an autocorrelation that has been conducted over a large range of time delay values τ. This method works by identifying the fringe peaks in the autocorrelation signal and fitting a gaussian to them. The amplitude of the gaussian may then be used to determine the amplitude of the autocorrelation signal. The challenge here is to accurately identify the fringe peaks in a noisy signal. The second method applies to autocorrelation measurements conducted close to the zero time delay $\tau = 0$. This method assumes that there is little variation in the envelope of the signal and is approximately sinusoidal. The amplitude is extracted by fitting a sinusoid to the signal.

2.5.1 Gaussian Fitting

To fit a gaussian to the envelope of an autocorrelation signal, one must identify the fringe maxima and minima in the signal. One method to do this is to identify the zero crossings of the first derivative of the signal. These are the locations of the extrema in the signal. One may then check if the second derivative is positive or negative to determine if the extrema belong to the lower or upper envelope: negative second derivative belongs to the upper envelope, positive belongs to the lower envelope. Gaussians may then be fitted using the method of least squares to the upper and lower extrema to determine the autocorrelation amplitude. Since the two gaussian envelopes share the same baseline, the amplitude of the autocorrelation signal is given by the sum of the amplitudes of the two gaussian envelopes. An example of this method on a modeled autocorrelation signal is presented in figure 2.3.

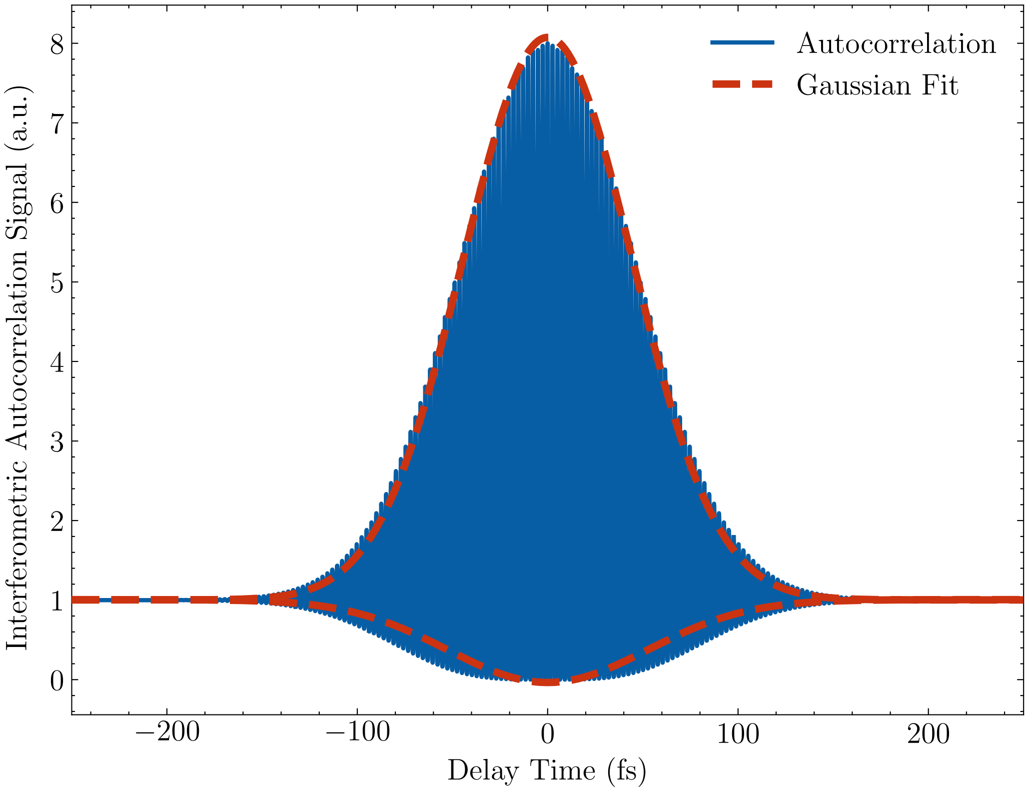

Figure 2.3: Gaussian envelope fit to a model autocorrelation signal. A gaussian was fit separately for the top and the bottom envelopes. While the bottom envelope is not a gaussian, the fitted gaussian can determine the amplitude of the background.

2.5.2 Sine Fitting

The second method applies to autocorrelation measurements that have been conducted over a small range of time delay values near $\tau = 0$. One may assume such a signal to have a constant amplitude, as there is little change in the envelope, and thus may be approximated by a sinusoid of the form

$$A \sin(\omega_0 \tau + \phi) + c, \tag{2.32}$$

where ω_0 is the carrier angular frequency of the pulses, A is the signal amplitude, ϕ is the phase, and c is a background offset. Fitting a sinusoid of the form given in equation 2.32 allows one to determine the amplitude A of the autocorrelation.

It was shown in figure 2.2 that an AFM autocorrelation may have a symmetric or asymmetric shape. To show that the sine fitting method can work for both the symmetric and asymmetric cases, figure 2.4 shows a sine fit to a modelled autocorrelation in each of these cases. The symmetric autocorrelation is of the form

$$S(\tau) \propto \int_{-\infty}^{\infty} |E(t) + E(t+\tau)|^2 \, dt, \tag{2.33}$$

while the asymmetric autocorrelation is of the form

$$S(\tau) \propto \int_{-\infty}^{\infty} \left(|E(t) + E(t+\tau)|^2\right)^2 dt, \tag{2.34}$$

as given in equation 2.18. In reality, it may be assumed that an AFM autocorrelation measurement will be some linear combination of these two cases. Figure 2.4 shows a sine fit to the most asymmetric case given by equation 2.34. Although there is a significant residual, the amplitude of the fit is 0.98, indicating that even in the most asymmetric case the amplitude can be accurately determined with the sine fit method.

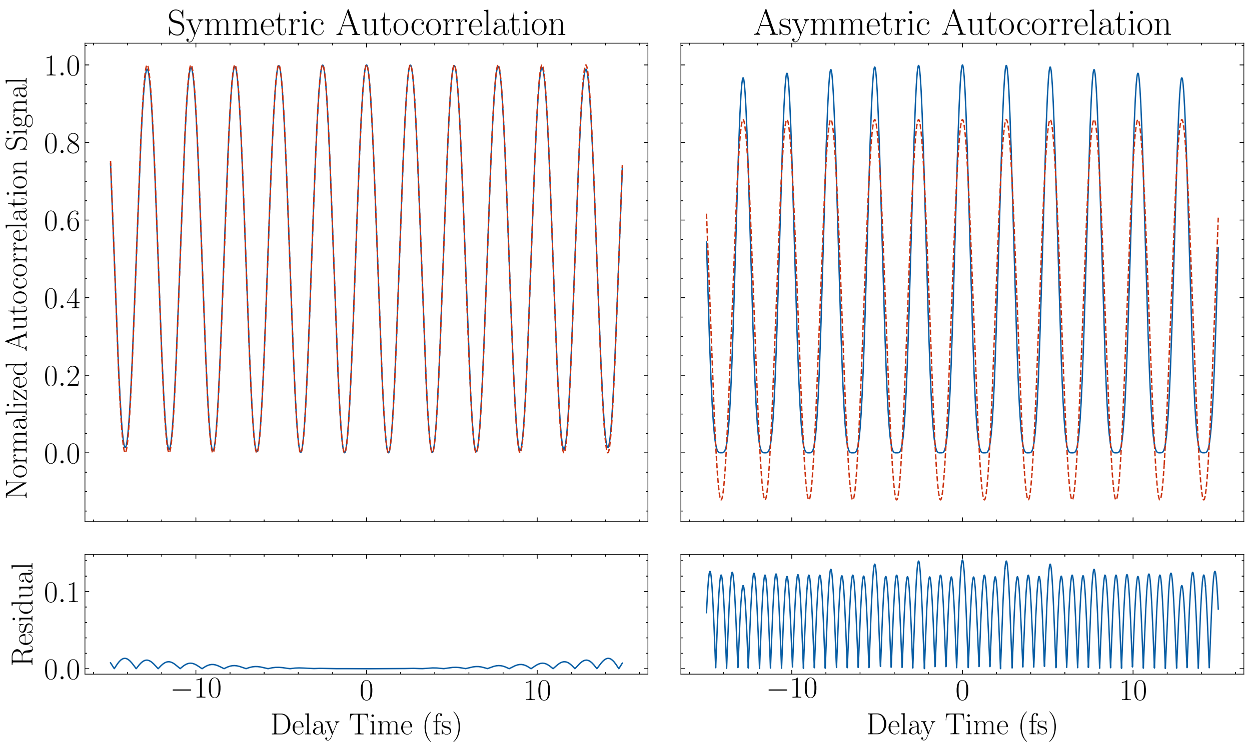

Figure 2.4: Sine fitted (dashed red curve) to an autocorrelation (solid blue curve) close to the zero time delay. The plot on the top left is the symmetric case described by equation 2.33, while the one on the top right is the most asymmetric case described by equation 2.34. The plots on the bottom show the residuals of the respective fits.

2.6 Noise Analysis

There are two advantages to the sine fitting method presented in section 2.5.2. One is that the autocorrelation measurement can be conducted more quickly due to the shorter delay time sweep. The other advantage is that one can measure the noise in the signal from the residuals of the sine fitting. This is useful as it allows one to correlate the noise present in the signal to the autocorrelation amplitude. In this section, autocorrelations will be modelled with noise proportional to $\sqrt{S(\tau)}$, $S(\tau)$, and $S(\tau)^2$, where $S(\tau)$ is the signal, and it will be demonstrated that the sine fitting method is capable of extracting information about the noise.

To model a noisy autocorrelation signal, noise was added to modelled signals like those shown in figure 2.4. To generate the noise, a random number is added to each data point in the signal, where the random number is of the form

$$\alpha \left|S(\tau)\right|^{p} x, \tag{2.35}$$

where x is a random number sampled from a standard normal distribution (mean 0 and variance 1), p is the power of $S(\tau)$ which the noise is proportional to, and α is a constant that can be used to set the signal to noise ratio. To extract the noise level from the noisy signal, a sine was fit to the signal near $\tau = 0$, and the standard deviation σ of the residuals was calculated to quantify the noise level. Figure 2.5 shows how the extracted σ (blue dots) scales with increasing amplitude of the signal $S(\tau)$, with $p = 0.5$, 1, and 2. The top row

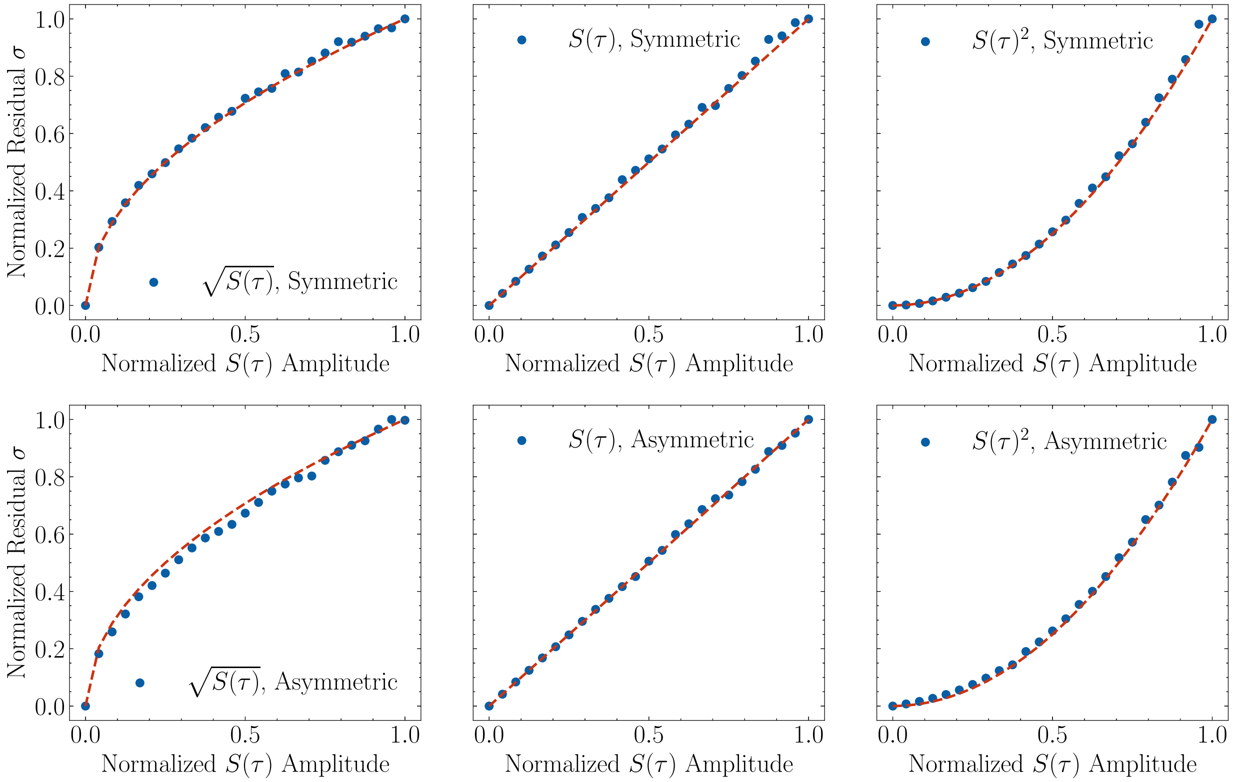

Figure 2.5: Residual σ of sines fit to noisy theoretical autocorrelations for varying autocorrelation amplitudes. Blue dots correspond to extracted σ, while red curves correspond to expected trends. The top row corresponds to the symmetric autocorrelation case, while the bottom row corresponds to the asymmetric autocorrelation case. Each column corresponds to a different power of $S(\tau)$ which the noise is proportional to. The x and y axes were normalized to range from 0 to 1.

of figure 2.5 was done for the symmetric autocorrelation described by equation 2.33, while the bottom row was done for the asymmetric autocorrelation described by equation 2.34. Comparing the extracted σ to the red curves in figure 2.5 shows that the sine fitting method can accurately quantify the noise level in a noisy autocorrelation signal. The deviation of the $\sqrt{S(\tau)}$ extracted noise from the expected curve in the asymmetric case may be explained by the relatively large residual shown in figure 2.4, which introduces a linear component to the trend.

One might argue that the source of the noise measured in the AFM may not be due to a sample effect. There are two other sources that must be considered: laser fluctuations and instabilities in the time delay τ between the laser pulses. Laser fluctuations are easily accounted for by normalizing the AFM signal with respect to the signal measured by the photodiode. The next chapter will go into more detail to show that these two signals are collected simultaneously in the experiment.

Instabilities in the time delay contribute noise to the measurement that have a different nature than noise related to the magnitude of the signal. To demonstrate this, an autocorrelation was modelled with fluctuations in the time delay, and fitted with a sine. The distribution of the residual is shown in figure 2.6a. The time delay noise distribution follows a more lorentzian distribution than a gaussian one, while the amplitude noise distribution is best fitted by a gaussian. The precise reasoning for this should still be investigated, but this shows that one can verify that the noise measured by AFM is not dominated by time delay instabilities by checking what the distribution looks like.

2.7 Samples Investigated

Two samples were investigated in this work. The first sample was a thin film of merocyanine dye HB238 on a glass substrate via spin coating, while the second sample was a WS_2 monolayer deposited on a sapphire substrate by chemical vapour deposition (CVD). The HB238

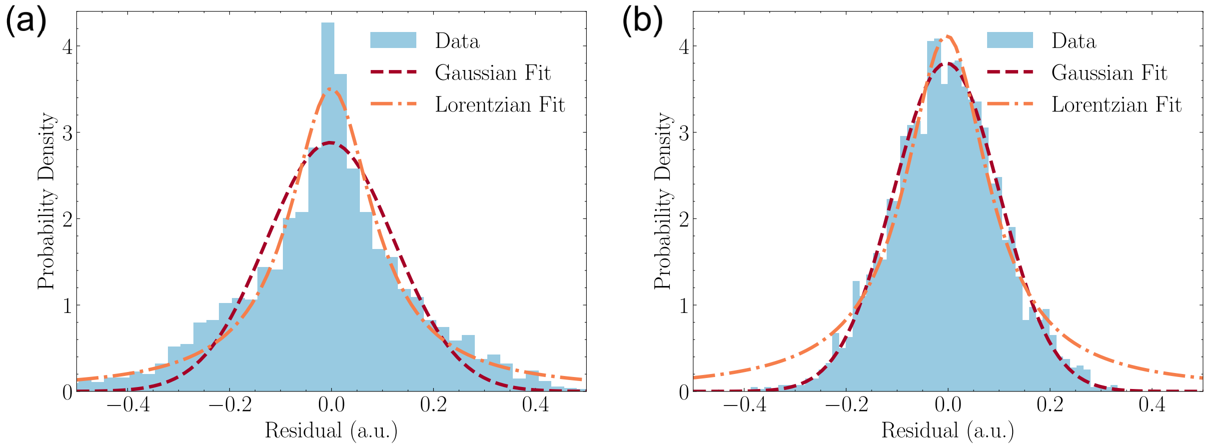

Figure 2.6: Noise distributions due to **(a)** time delay instability and **(b)** amplitude noise. Both distribution were fitted with a gaussian and lorentzian. A residual sum of squares test was performed to determine which fit was better in each case. The time delay noise distribution is better fitted by a lorentzian, while the amplitude noise is better fitted by a gaussian.

sample was manufactured by Professor Meerholz's group at the University of Cologne, and the WS_2 sample was manufactured by Dr. Goh's group at A*STAR.

Merocyanine dye HB238 is an organic compound with a non-centrosymmetric structure [34, 35]. The HB238 sample used here was previously studied by Spiegelberg, who showed that it has a nonlinear response when probed by ultrafast AFM [26]. This sample was used in this work to reproduce previous results and to demonstrate that the experimental method works. The HB238 sample was manufactured by spin-coating a 24 nm layer of the dye onto a glass substrate, and then annealed at 150°C. The annealing process aligns the HB238 molecules and results in the film having a greater optical response [36].

The HB238 sample used here was initially manufactured in 2022. To verify that the sample has not degraded over time, ultraviolet-visible (UV-vis) spectroscopy was conducted and compared to reported spectra of new samples manufactured by the same group, as shown in figure 2.7 [36]. The alignment of the measured UV-vis peak of the old sample with the reported peak of a new sample in [36] indicates that old sample has remained intact and is likely to still have a strong nonlinear response detectable by ultrafast AFM. The ultrafast AFM measurements will be shown in chapter 4.

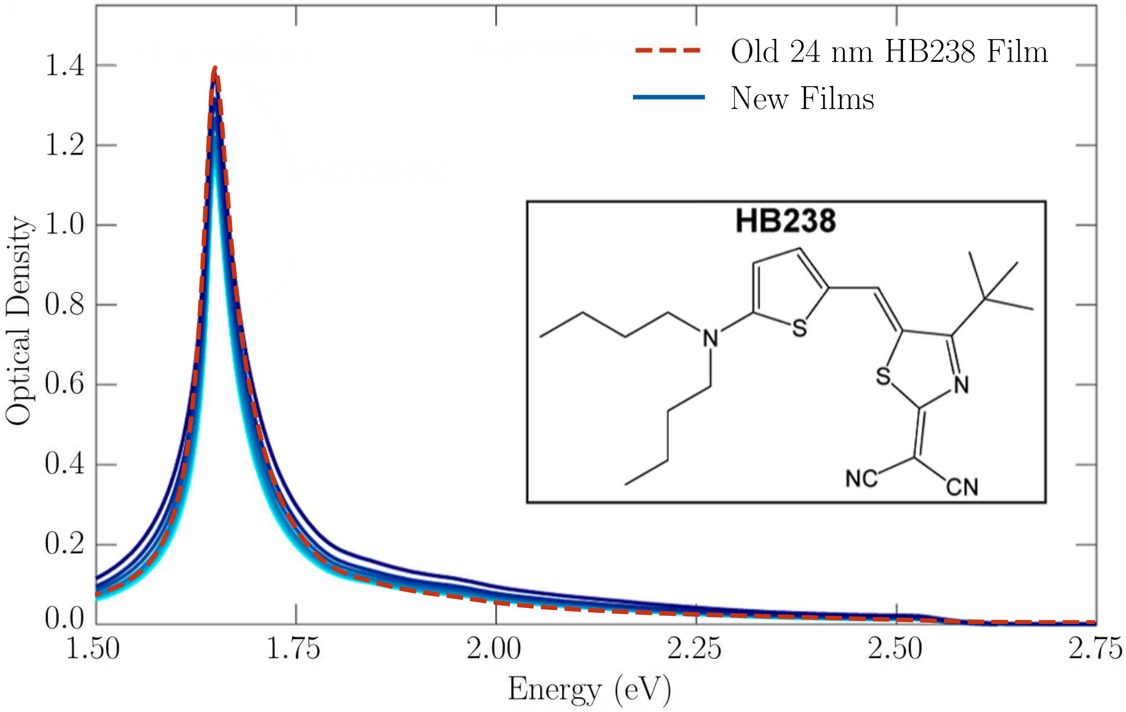

Figure 2.7: UV-vis spectra of spin-coated HB238 films on glass substrates. The UV-vis spectrum that was measured on the old sample (dashed red line) was overlayed on the spectra reported by [36] (solid blue lines), showing that the main peak is at the same energy. The inset shows the structure of the HB238 molecule. Figure adapted from [36].

Monolayer WS_2 was also studied as it also has a strong nonlinear optical response, with $\chi^{(2)}$ on the order of 1 nm/V [37, 38]. This is an extremely large $\chi^{(2)}$, as $\chi^{(2)}$ values of materials typically used for SHG, such as beta barium borate (BBO), are on the order of 1 pm/V [23]. The WS_2 sample used in this work was grown on a sapphire substrate via CVD, and was grown to form islands of monolayer WS_2 rather than a uniform coverage. A nonuniform sample like this is important to show the spatial correlation between autocorrelation amplitude and noise measurements with ultrafast AFM, as one can compare measurements conducted on the WS_2 flakes with those done on the substrate. Such a spatial measurement will be shown in chapter 4.

Chapter 3

Experimental Methods

Ultrafast atomic force microscopy (AFM) for nonlinear optical measurements relies on the coupling of an ultrafast laser system and an AFM. In this chapter the well understood commercial AFM system will be briefly discussed, and the remainder of the chapter will discuss the optical system and how it is coupled to the AFM. The characterization of the signal measured by AFM will be discussed at the end.

3.1 The AFM System

The AFM used in this work is a room temperature modified commercial JEOL JSPM-4500A ultra-high vacuum (UHV) system. The UHV system consists of three chambers: a loadlock for transferring tips and samples in and out of vacuum, a preparation chamber for sample processing (such as annealing, cleaving, or molecular evaporation), and a measurement chamber which houses the AFM.

The base pressures of the preparation and measurement chambers is on the order of 10^{-11} mbar. This pressure is primarily maintained by ion pumps (one connected to each chamber), which ionize unwanted gas molecules and subsequently accelerate the molecules through an electric field towards a cathode. The molecules strike the cathode and become buried within it, resulting in a lower pressure in the chamber.

The AFM used in this system works on the basis of frequency modulated (FM) AFM, as discussed in chapter 2. The cantilevers used in this work are metal-coated silicon cantilevers from Nanosensors (PPP-NCHPt). These cantilevers have a resonance frequency of about 250-300 kHz, a spring constant of about 30-50 N/m, and a Q factor of around 20 000 in UHV. These values vary from cantilever to cantilever, but are well known for each one. The metal coating of the tip enhances its electrical conductivity. The cantilever is oscillated by a piezo, and the deflection is measured by beam deflection system including a 670 nm laser and a four-quadrant photodiode setup. An optical bandpass filter is placed over the photodiode to prevent signal contamination by ambient light or the ultrafast laser used for optical measurements. The cantilever oscillations are controlled via a phase-lock loop (PLL) in a Nanonis scanning probe microscopy (SPM) controller.

The sample in the AFM is placed in a piezo-driven stage that has a scan range of about 4.5 × 4.5 µm in the *xy*-plane. Additionally, the stage may be moved with coarse motors over an area of 2 × 2 mm in the *xy*-plane. The AFM tip is brought into proximity with the sample surface with a combination of a coarse and a piezo motor until the frequency shift setpoint is detected.

3.2 Optical System

To generate laser pulses, a Toptica FemtoFibre pro near-infrared laser system is used. The system consists of an erbium fibre laser to generate 100 fs pulses at 1560 nm, with a repetition rate of 80 MHz at an average power of 350 mW. A second harmonic generation unit is used to also output 100 fs pulses at 780 nm with an average power of 140 mW. Unless otherwise specified, all experiments here are done with the 780 nm output.

A Mach-Zehnder interferometer is used to control the delay time between subsequent pulses, as shown in figure 3.1 [39, 40]. In the interferometer, the output beam from the laser system is passed through a beam splitter into two beams. One of the beams has a

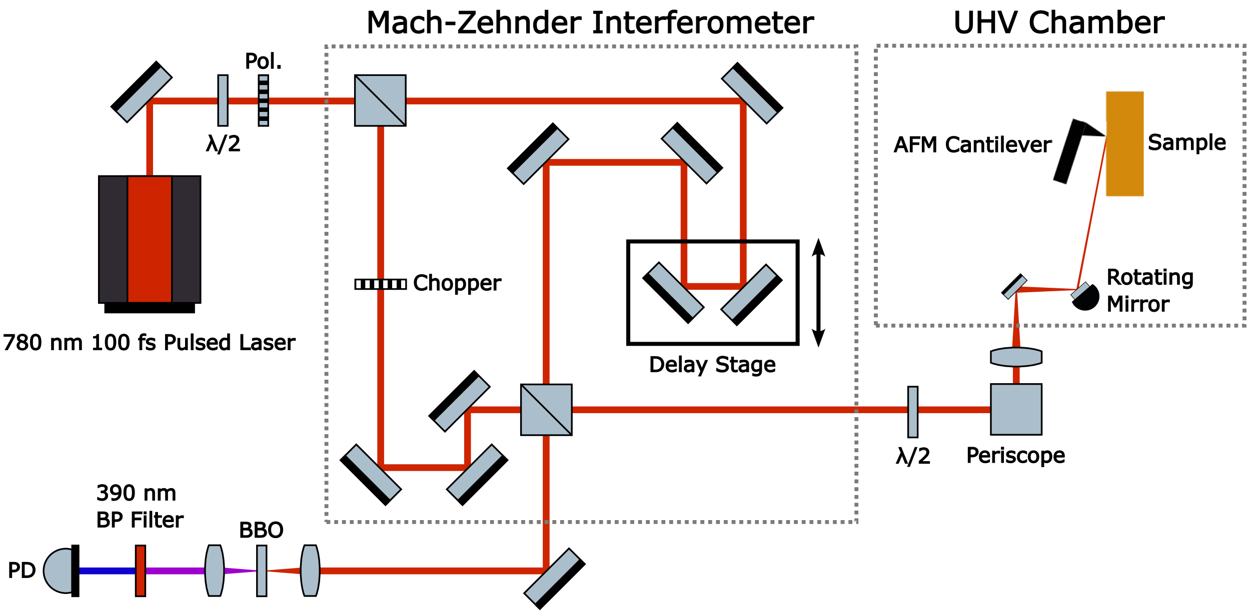

Figure 3.1: Schematic of the optical setup used for measuring nonlinear optics with AFM. A Toptica FemtoFibre Pro NIR laser system is used to generate 100 fs pulses with a carrier wavelength of 780 nm at a repetition rate of 80 MHz. The intensity of the laser is controlled via a half-wave plate and polarizer setup, where the polarizer is fixed and the wave plate is rotated. A Mach-Zehnder interferometer is used to control the delay time between subsequent pulses. The delay stage used is a Thorlabs DDS220 linear translation stage, which has a minimal incremental movement of 0.1 µm (0.33 fs). The two arms of the interferometer are recombined colinearly. One output of the interferometer gets focused onto a BBO crystal, and the second harmonic light is detected via a photodiode. The photodiode is used to monitor the alignment of the beams and laser fluctuations. The second output of the interferometer is fed into the UHV chamber with a periscope. A half-wave plate is used to control the polarization of the beam. The beam is focused onto the sample, and a rotating mirror is used to direct the beam into the AFM tip-sample junction. Note: Figure not to scale.

corner reflector mounted on a ThorLabs DDS220 translation stage to control the time delay between the pulse copies. The two beams from the interferometer are recombined at a second beam splitter, where one copy of the pulses (known as the photodiode branch) is sent through a β-barium borate (BBO) crystal and into a photodiode, while the other copy (known as the AFM branch) is sent into the UHV-AFM system where it is aligned with the sample. The main purpose of the photodiode branch is for interferometer alignment and to have a reference signal which the AFM signal is compared to. The photodiode is also able to monitor any laser fluctuations. The BBO crystal in the photodiode branch is used for second harmonic generation [41]. The photodiode used is a reverse biased silicon photodiode, and the current signal is amplified by a Femto DLPCA-200 low noise transimpedance amplifier. The output voltage signal from the amplifier is recorded by the Nanonis SPM control system.

3.2.1 Beam Alignment

As was discussed in section 2.3, an interferometric autocorrelation measurement has an 8:1 ratio. When aligning the interferometer, autocorrelation measurements with the photodiode branch were conducted to check the accuracy of the alignment. The general procedure to align the interferometer is as follows:

1. Align both interferometer beams to pass through the irises on the photodiode branch. For good overlap of the two beams, it is critical that the beams pass through the irises with equal intensity.

2. Insert a convex lens after the first iris. Then place the BBO crystal in the focal point after the lens. One can move the BBO crystal by hand along the beam path until the photodiode signal is maximized. Once the best position is found, adjust the angle of the BBO crystal in the plane normal to the beam path until the photodiode signal is maximized.

3. Make very fine adjustments to the interferometer mirrors until an 8:1 ratio is achieved in the photodiode autocorrelation measurement.

The following paragraphs detail how misalignments will influence the amplitude ratio of the autocorrelation measurement.

Uneven Beam Intensities

If one attempts an interferometric autocorrelation with beams of uneven intensities, the resulting autocorrelation will not have an 8:1 ratio. This might happen if one of the beams is passing through a dirty optical element or gets clipped at the edge of an optical element. To demonstrate how significant of an effect this can have on the autocorrelation ratio, autocorrelations were modelled with one of the pulses attenuated. Figure 3.2 shows the resulting autocorrelation ratios as a function of the beam intensity ratios. The autocorrelation ratio is not significantly affected if the ratio of the beam intensities is greater than about 0.85, but it starts to deteriorate quickly below 0.8.

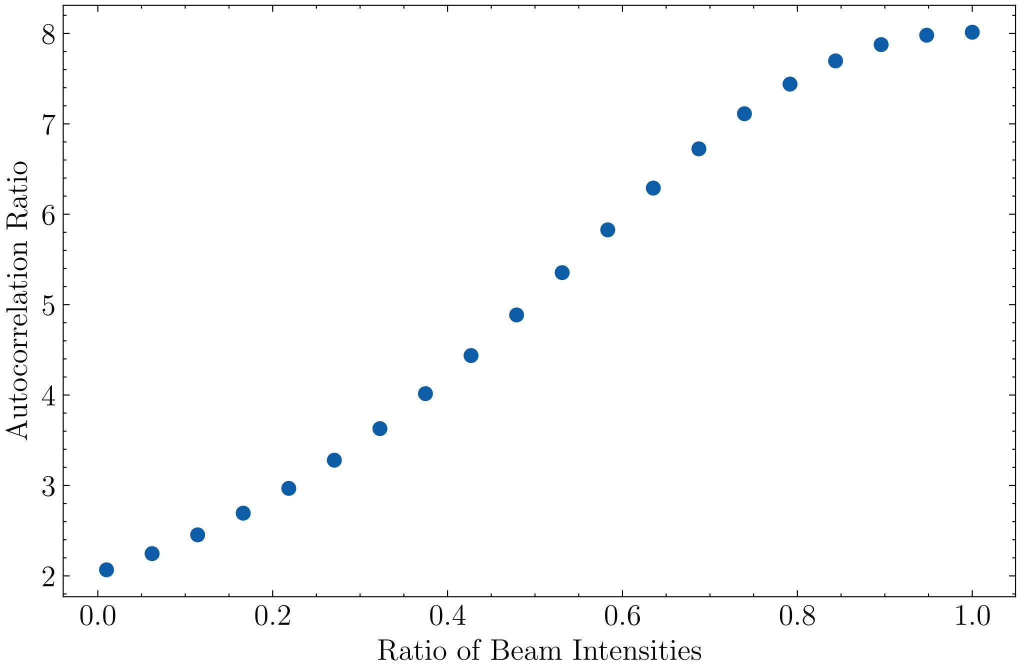

Figure 3.2: Effect of uneven beam intensities on interferometric autocorrelation ratio. To achieve the desired 8:1 ratio of an interferometric autocorrelation, one must ensure that the two beams of the interferometer are similar in intensity. If the ratio of the intensities is around 0.85 or greater, then a good autocorrelation ratio will be achieved. Once the ratio of the intensities falls below 0.8, then the autocorrelation ratio will quickly decrease.

BBO Crystal Angle Tuning

As discussed in chapter 2, phase matching is critical for efficient generation of second harmonic light in a nonlinear optical crystal. Phase matching refers to matching the phase velocity of the fundamental beam (the input beam with frequency ω) to that of the generated second harmonic beam. When the phase velocities are perfectly matched, the second harmonic beam will constructively interfere with newly produced second harmonic light as it travels in phase with the fundamental beam through the crystal, resulting in amplification of the second harmonic beam. If the phase velocities are not matched, the second harmonic will interfere deconstructively with newly produced second harmonic light, ultimately resulting in a low intensity of second harmonic light [23].

Phase matching, or angle tuning, is done by adjusting the angle between the propagation axis of the fundamental beam and the optical axis of the crystal. In this setup, a thin (< 100 µm) BBO crystal is used to generate second harmonic light. The BBO crystal was polished so that incident 780 nm light normal to the surface is already phase matched.

In the case of linearly polarized light, as is the case in this work, the orientation of the BBO about the propagation axis of the fundamental beam must also be tuned to maximize SHG. Here, the BBO was mounted in a rotation stage allowing rotation in the plane normal to the propagation axis. The stage was incrementally rotated until the second harmonic light detected by the photodiode was maximized.

First Harmonic Leakage

An interferometric autocorrelation requires only the second harmonic light to be passed into the photodiode. Thus, a bandpass filter is placed after the BBO crystal to filter out the first harmonic light. In this setup, the first harmonic light has a wavelength of 780 nm, and the second harmonic has a wavelength of 390 nm. A ThorLabs FBH390-10 bandpass filter was used, which ThorLabs reports has a 0.0001% transmission of 780 nm light and a 94.7% transmission of 390 nm light. Although the transmission of 780 nm light is extremely small, the first harmonic beam has much greater intensity than the second harmonic beam, leading to first harmonic leakage that is significant enough to affect the measured interferometric autocorrelation. It was found that placing a second bandpass filter improves the ratio of the interferometric autocorrelation. Figure 3.3 shows that placing a second bandpass filter improves the autocorrelation ratio from 6.7 to 7.9.

While a second filter can help reduce direct leakage of the first harmonic, there may be

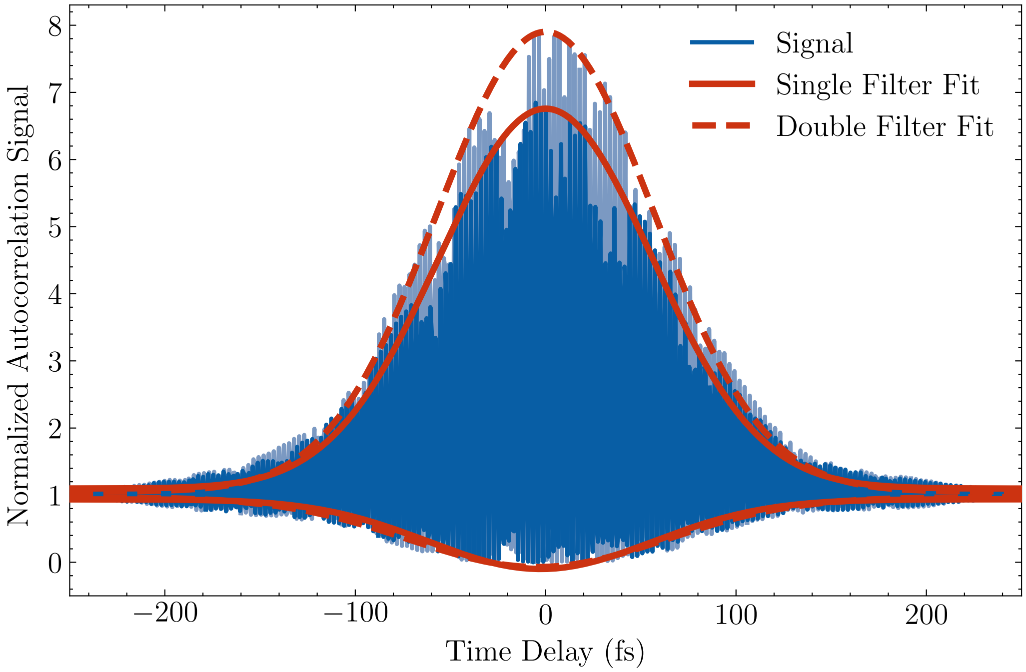

Figure 3.3: Normalized interferometric autocorrelations with one and two bandpass filters. An autocorrelation conducted with some first harmonic leakage will produce a signal below the desired 8:1 ratio, as seen in the dark blue signal, which has a ratio of 6.7. Using two bandpass filters improves the ratio to 7.9, as seen in the light blue signal. The envelopes of the signals were fitted with a gaussian to accurately determine the ratio. Some of the fringes of the autocorrelations are missing because the delay step was slightly larger than the width of the fringe.

some background scattering of first harmonic light that finds its way into the photodiode, such as by reflecting off the backside of the bandpass filter. To prevent any stray light hitting the photodiode, a tube was placed between the photodiode and second bandpass filter, so that the only light hitting the photodiode was passed through the filter.

An accurate measurement of the interferometric autocorrelation is important for monitoring the alignment of the interferometer beams and laser fluctuations. Minimizing first harmonic leakage into the photodiode ensures a more accurate interferometric autocorrelation measurement.

3.2.2 Polarization Rotation in Periscope

It is known that p-polarized light relative to the plane of the sample in the AFM maximizes the nonlinear optical signal detected by AFM [25]. The output polarization of the laser is s-polarized with respect to the plane of incidence of the optical table (parallel to the optical table plane). Considering that in this system the plane of the sample is perpendicular to the plane of the optical table, one might assume that these two polarizations are in the same plane. However, one must carefully consider what happens to the polarization of the beam as it is directed into the AFM.

When the laser beam reflects from a mirror, the polarization relative to the plane of incidence remains constant. If the beam is reflected by two consecutive mirrors that do not share the same plane of incidence, the polarization of the beam may rotate into a different plane than that of the initial beam. Such is the case when the beam passes through the second periscope that guides the beam into the UHV chamber, as the top mirror is rotated 90° relative to the bottom mirror. Figure 3.4a illustrates what happens to the polarization as the beam passes through a 90° periscope. It is possible to avoid this problem by adding an additional mirror as illustrated in figure 3.4b, but various constraints may

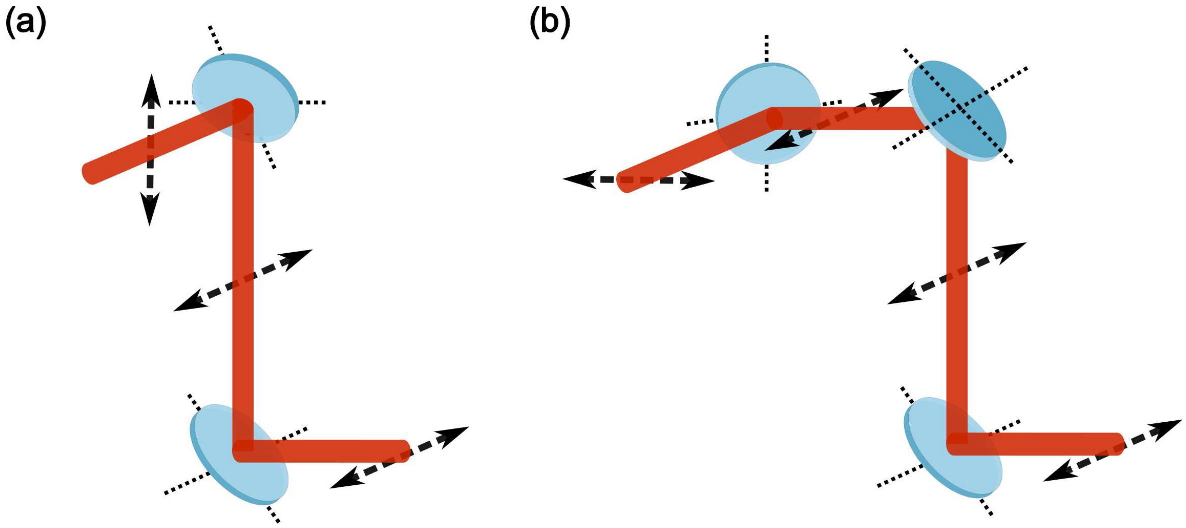

Figure 3.4: The effect of a periscope on laser beam polarization. **(a)** A 90° periscope will rotate the beam polarization. **(b)** A straight periscope with an additional mirror maintains the polarization parallel to that of the input beam.

prohibit this. Alternatively, as was done in this setup, a half-wave plate may be used to rotate the polarization back as desired.

3.3 Ultrafast AFM

The Mach-Zehnder interferometer has two output beam lines: one directed to the photodiode, and the other directed into the UHV chamber, where the beam is focused with an achromatic doublet lens into the tip-sample junction at an angle of about 80°. The spot size on the sample is estimated to be 900 by 200 µm. To align the laser beam with the tip-sample junction, a rotating mirror moved by piezo motors inside the UHV chamber is used to control the beam direction. The beam spot location is known by first looking into the chamber with cameras. Once the beam is close to the AFM cantilever, the chopper in one of the Mach-Zehnder interferometer arms is turned on. The final adjustments of the alignment are done by maximizing the chopper frequency peak in the power spectral density (PSD) of the frequency shift channel of the AFM. The peak is a result of thermal fluctuations in the cantilever induced by the chopping of the beam. The beam is directly aligned with the cantilever when this peak is maximized. The rotating mirror is then finely rotated to direct the beam at the sample below the AFM tip. The mirror is rotated until the chopper peak disappears from the frequency shift PSD.

While the laser used in the experiments presented here is primarily directed towards the sample area around the tip-sample junction to minimize thermal driving of the AFM cantilever, it is inevitable that some of the laser will be incident on the cantilever and tip. The thermal effects of a laser incident on an AFM tip are discussed in depth by Milner et al. (2010) in [42]. They show that the thermal effects induced on the tip is heavily dependent on the alignment of the laser with the cantilever/tip. For example, they showed that in two different laser alignments the laser power varied by a factor of 2, while the tip temperature was the same. Hence what matters in such thermal considerations is the laser fluence rather than the total laser power.

One can verify that the signal measured by the AFM during a delay sweep is a surface effect rather than a thermal effect by comparing sweeps in approached and retracted tip positions. Figure 3.5 shows AFM autocorrelation amplitudes at various intensities, at both the approached and retracted tip positions. The z-feedback was turned off for each measurement so that the autocorrelation signal is measured in the frequency shift channel. The approached measurement was done on a CVD grown WS_2 flake on a sapphire substrate. Measurements on this sample will be discussed in greater detail in the next chapter. The autocorrelation in the approached position has a much larger signal than that in the retracted position, indicating that the measured signal is indeed due to surface effects rather than a thermal effect. One should note that the approached and retracted positions are less than 1 µm apart, so the tip is not moving in and out of the laser beam when moving between these positions.

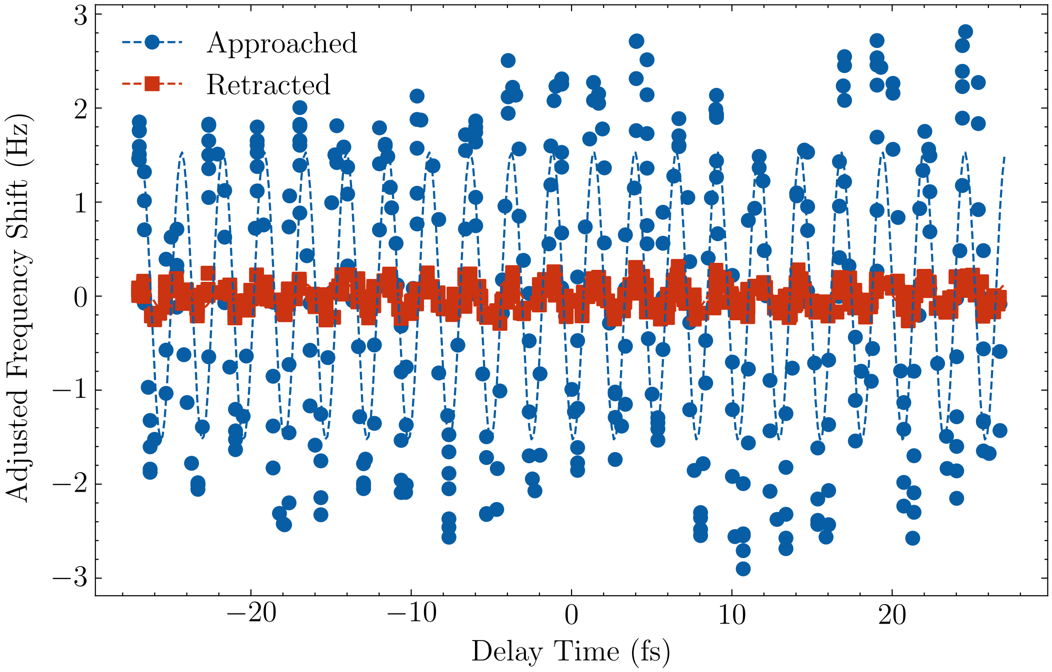

Figure 3.5: Autocorrelation measurements with approached and retracted AFM tip positions at full laser intensity. The background frequency shift was subtracted from the data.

3.3.1 Verifying Nonlinear Optical Effects

Once the beam is aligned with the tip-sample junction, one must determine if the measured signal is a nonlinear effect or not. A nonlinear process will have a nonlinear dependence on the laser power. To demonstrate that a nonlinear process is indeed being measured with the AFM during an autocorrelation, measurements were conducted at various laser intensities at a constant tip height (z-feedback off for all measurements), shown in figure 3.6. This measurement was done with the merocyanide dye HB238 sample discussed in section 2.7 in order to verify that the experimental setup was working. The intensity is varied with a rotating half-wave plate and a fixed polarizer, which works on the basis of Malus' law:

$$I = I_0 \cos^2 \theta, \tag{3.1}$$

where I_0 and I are the initial and final intensities, respectively, and θ is the angle of the polarizer axis relative to the polarization of the initial beam. The laser intensities used in this measurement were first recorded with the photodiode with the bandpass filter removed.

In order to prevent possible tip height changes due to thermal effects, the laser intensity was not varied in a monotonous fashion. Instead, the initial intensity was set to be around the average of the desired intensity range. Subsequent intensities were alternated below and above the initial intensity in order to minimize compounding thermal effects on the tip.

The top plot in figure 3.6 shows the autocorrelation amplitudes at various laser intensities. The blue data points were done with the tip approached over a CVD grown WS_2 flake. The blue data points have a quadratic trend, indicating nonlinear optical effects are measured at the surface. To show that thermal effects do not contribute to any nonlinear measurements, the measurements were repeated with the tip retracted and the laser fully aligned with the cantilever to maximize thermal effects, shown in the red data in figure 3.6. Not only does the thermal effect here have a smaller magnitude than the surface effects at higher intensities, but these measurements also have a linear trend, indicating that they do not contribute to any nonlinear effects. The thermal contributions to the autocorrelation amplitude are likely due to thermal expansion of the cantilever dimensions. The spring constant k of the cantilever are dependent on the cantilever dimensions, thus any changes to the dimensions will result in changes to k and also the resonance frequency [43].

3.3.2 Measuring Nonlinear Optics with Noise

The bottom plot of figure 3.6 shows the noise extracted from the measurements shown in the top plot. As discussed in chapter 2, the noise was extracted by fitting a sinusoid to the autocorrelation measurement close to zero time delay and finding the standard deviation of the residuals. To verify that the residuals are a good indicator of the noise present, histograms of the residuals were plotted for each autocorrelation measurement and fitted with a gaussian. An example of this is shown in figure 3.7. For each histogram, it was verified that the residuals had a gaussian distribution, and that the distribution was centred at zero. This indicates that the noise is not biased, and that it is not a result of time delay fluctuations as was discussed in section 2.6.

In figure 3.6, the noise of the approached measurements scales quadratically with laser intensity, just like the amplitudes. This means that the noise is proportional to the amplitude, and it can be used to characterize the second order susceptibility $\chi^{(2)}$ just like the amplitude. The benefit of using noise to characterize $\chi^{(2)}$ is that it can be measured much quicker than the autocorrelation amplitude. Each autocorrelation measurement shown in figure 3.6 took about 8 seconds. Noise, on the other hand, could be measured via a simple frequency shift time trace in a fraction of a second.

The next chapter will demonstrate how these measurements are conducted spatially over a sample, and will aim to show that noise measurements can be used to characterize local $\chi^{(2)}$ just like full autocorrelation measurements.

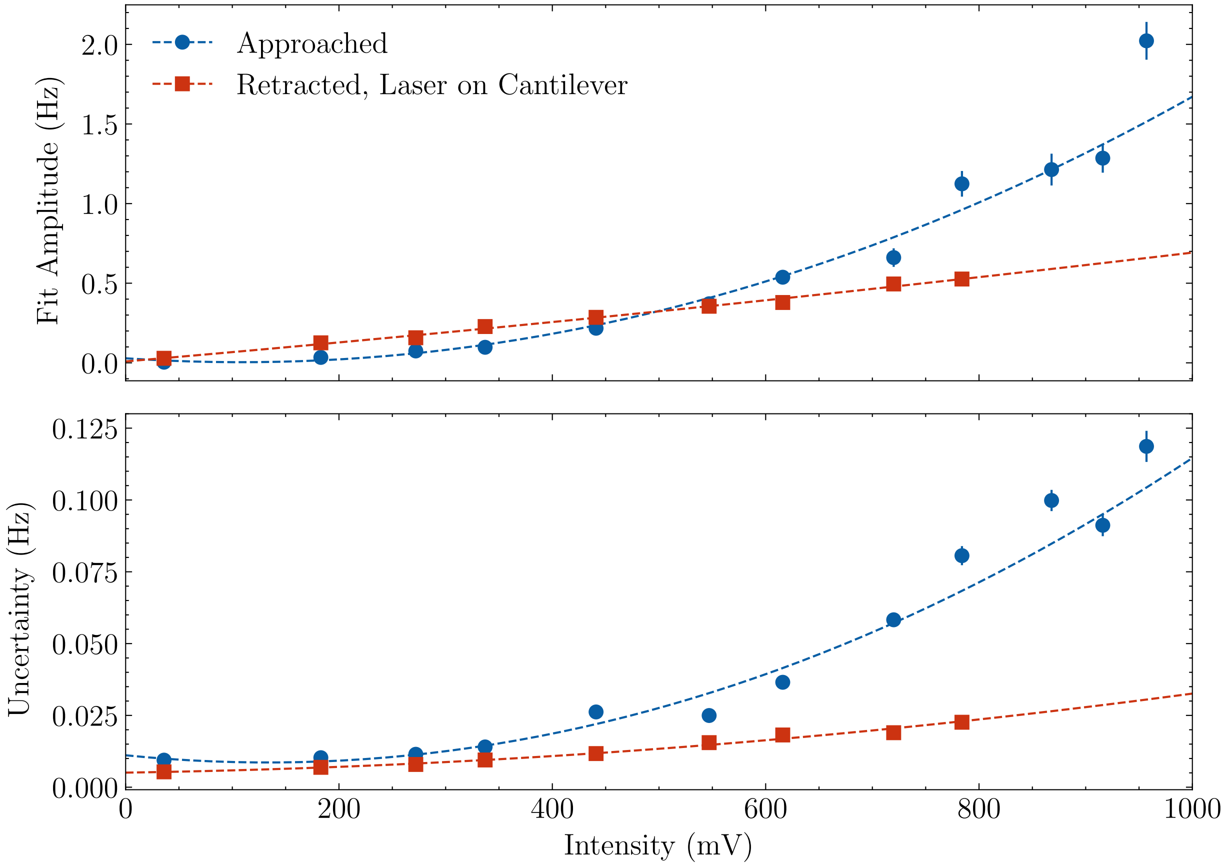

Figure 3.6: AFM autocorrelation measurements with varying laser intensity. The top plot shows the amplitudes of autocorrelations done with the tip approached over the HB238 film (blue dots) and retracted (red squares). The retracted data points were collected with the laser fully aligned with the cantilever to show the behaviour of thermal effects with varying laser intensity. The bottom plot shows how the noise scales during the measurements shown in the top plot. The noise here is the standard deviation of the residues of the sine fit of the autocorrelation measurement close to the zero time delay. The uncertainties in the noise were found via a statistical bootstrapping scheme. All of the data sets were fitted with a second order polynomial.

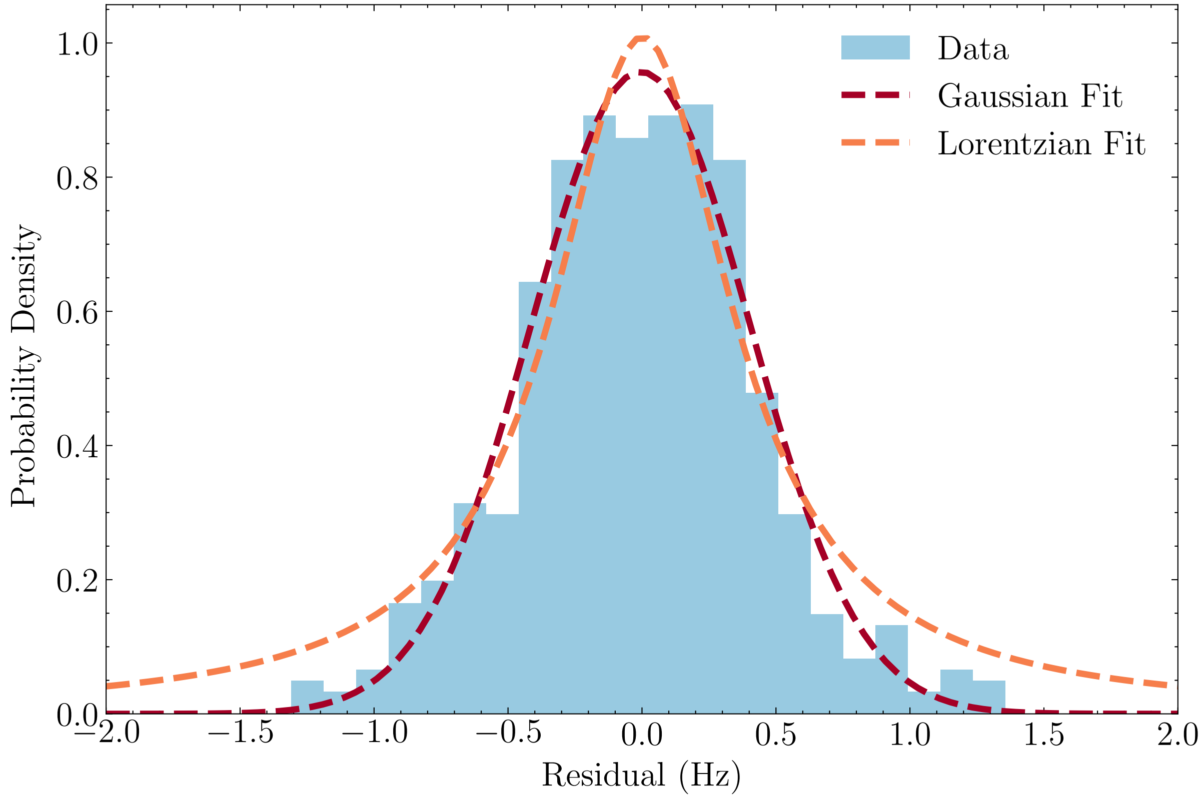

Figure 3.7: Histogram of residuals of a sine fit to an autocorrelation measurement. The residuals have a gaussian distribution centred at zero, as indicated by the gaussian fit, indicating that the residuals are a good indicator of the noise in the signal. The noise level in the signal may be quantified by the standard distribution of the residuals. Here, the bin heights of the residual counts were normalized to form a probability density. A lorentzian fit is also plotted to show that the source of the noise is not due to time delay fluctuation as was shown in section 2.6.

Chapter 4

Ultrafast AFM Measurements

The samples that were investigated in this work were merocyanine dye HB238 and CVD grown WS_2 flakes on sapphire, as was discussed in section 2.7. The HB238 sample was used in section 3.3.1 to reproduce results reported by Spiegelberg [26] and demonstrate that the experimental setup was indeed measuring nonlinear effects.

Now that it was confirmed that the setup was working, spatial measurements can be performed on the WS_2 sample, which will be discussed in this chapter.

4.1 Monolayer WS_2 on Sapphire Substrate

As mentioned in the first chapter of this work, 2-dimensional transition metal dichalcogenides (2D TMDs) exhibit second harmonic generation (SHG) properties. Sapphire is a centrosymmetric crystal, hence it does not cause SHG in the bulk. However, SHG can occur at the sapphire surface where the centrosymmetric geometry is broken, especially on r-cut sapphire [44]. Thus, one must carefully conduct measurements on WS_2 grown on sapphire to be able to distinguish between the flake and the substrate signals. Figure 4.1 shows the topography and bias channels of a KPFM scan taken of a WS_2 flake from this sample. As will be shown in section 4.1.1, the amplitude of the autocorrelation measured by AFM is dependent on the tip-sample separation. Thus it is necessary to ensure constant tip-sample separation when

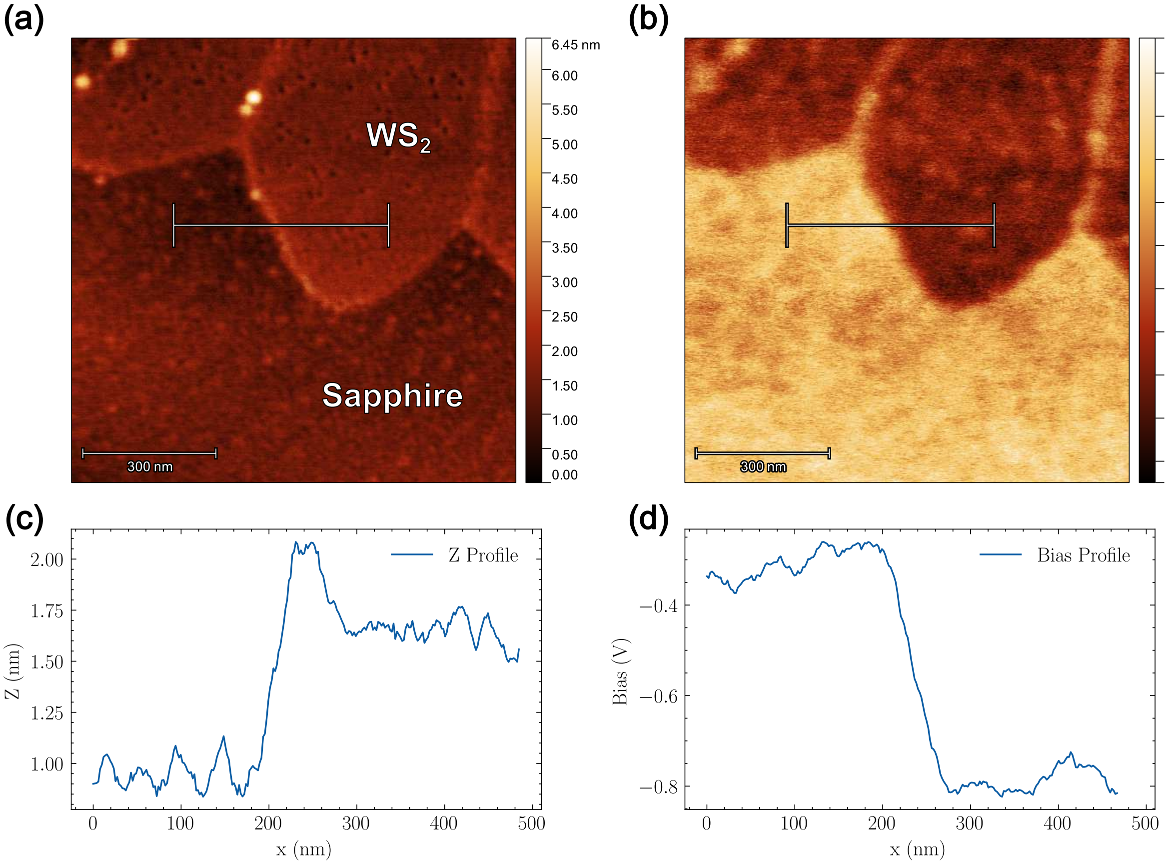

Figure 4.1: KPFM scan of a WS_2 flake on a sapphire substrate with no incident laser. **(a)** Topography and **(b)** bias channels of a KPFM scan taken of a WS_2 flake. **(c-d)** Line profiles shown in the topography and bias channels, respectively. These profiles are averaged over the width of the regions indicated by the bars in (a) and (b). The topography profile shows that the "inland" region of the WS_2 flake is approximately 0.7 nm higher than the sapphire substrate.

conducting spatially resolved nonlinear optical measurements. The topographical line profile in figure 4.1c shows that the surface of the WS_2 flake is approximately 0.7 nm higher than the sapphire substrate, which is consistent with reported monolayer WS_2 thicknesses [45]. Additionally, there is a significant difference in CPD values over the two regions, as shown in figure 4.1b, d.

4.1.1 Autocorrelation Amplitude vs Tip Height

The AFM autocorrelation signal is of electrostatic nature as was discussed in section 2.4, and thus is dependent on the tip-sample separation. Hudlet states the electrostatic force F_{elec} acting on the AFM tip is dependent on the tip-sample separation z via

$$F_{\mathrm{elec}} = \pi\varepsilon_0 V^2 \left[\frac{R^2}{z[z+R]} + \dots\right], \tag{4.1}$$

where $V = V_{\mathrm{cpd}} - V_{\mathrm{dc}}$ is the difference between the contact potential difference V_{cpd} and the applied bias V_{dc}, R is the tip radius, and z is the tip-sample separation [46]. The frequency shift Δf measured by FM-AFM given in equation 2.5 is

$$\Delta f \approx -\frac{\omega_0}{4\pi k}\frac{dF_{\mathrm{ts}}}{dz}, \tag{4.2}$$

with F_{ts} being the tip-sample force. Inserting F_{elec} from equation 4.1 results in the frequency shift to be approximately

$$\Delta f \propto \pi\varepsilon_0 V^2 \left[\frac{R^2(R+2z)}{z^2(z+R)^2}\right]. \tag{4.3}$$

Figure 4.2 shows the AFM autocorrelation amplitude and the amplitude uncertainty as a function of z on both the WS_2 flake and the sapphire substrate. The z values were recorded from the z piezo position. Since the z piezo position is only a relative value rather than an absolute measurement of the tip-sample separation, the z variable in equation 4.3 was redefined to be $z - z_0$, where z is the piezo position and z_0 is the position of the surface. The electrostatic model that was fitted to the AFM autocorrelation z spectra is

$$\Delta f = A\left[\frac{R^2\left(R+2\left(z-z_0\right)\right)}{\left(z-z_0\right)^2\left(z-z_0+R\right)^2}\right], \tag{4.4}$$

with the proportionality constant A and the surface position z_0 being fitted parameters. The PPP-NCHPt cantilevers from Nanosensors used in this measurement have a reported

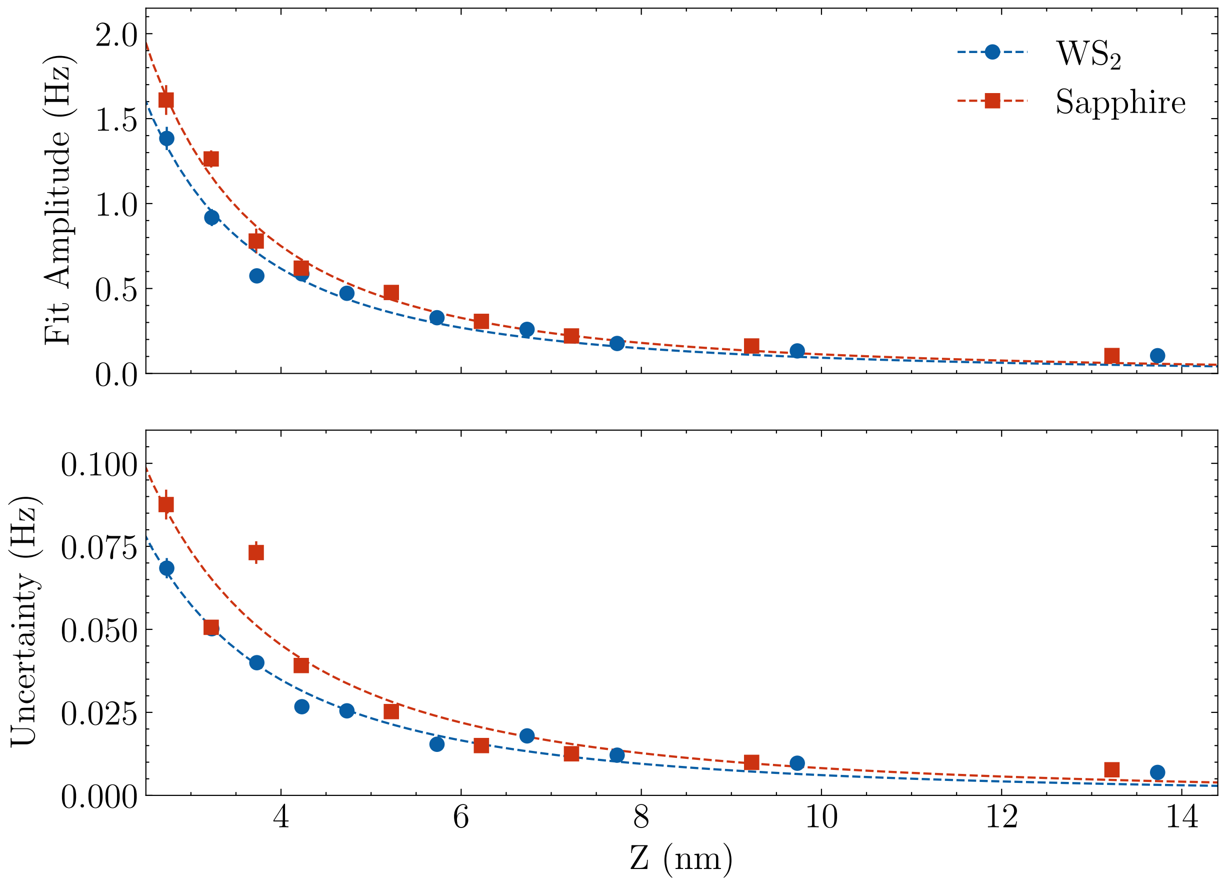

Figure 4.2: z spectra of autocorrelation amplitude and noise over WS_2 and sapphire. The spectra were fitted with Hudlet's electrostatic model [46]. The x axis of the plots corresponds to the tip-sample separation predicted by the model.

tip radius of curvature of $R = 25$ nm. Since the position of the surface did not change between these two z spectra, z_0 was shifted to zero for both fittings, so that the x-axis in figure 4.2 corresponds to the tip-sample separation.

4.1.2 Autocorrelation Amplitude and Noise vs Laser Power

To confirm that the signal measured with ultrafast AFM is of nonlinear nature, intensity measurements were conducted as discussed in section 3.3.1. Such measurements were conducted both on the WS_2 flakes and on the sapphire substrate, as shown in figure 4.3. As it was discussed in the previous section, it is critical to maintain a constant tip-sample separation when conducting nonlinear ultrafast measurements in different locations on the sample.

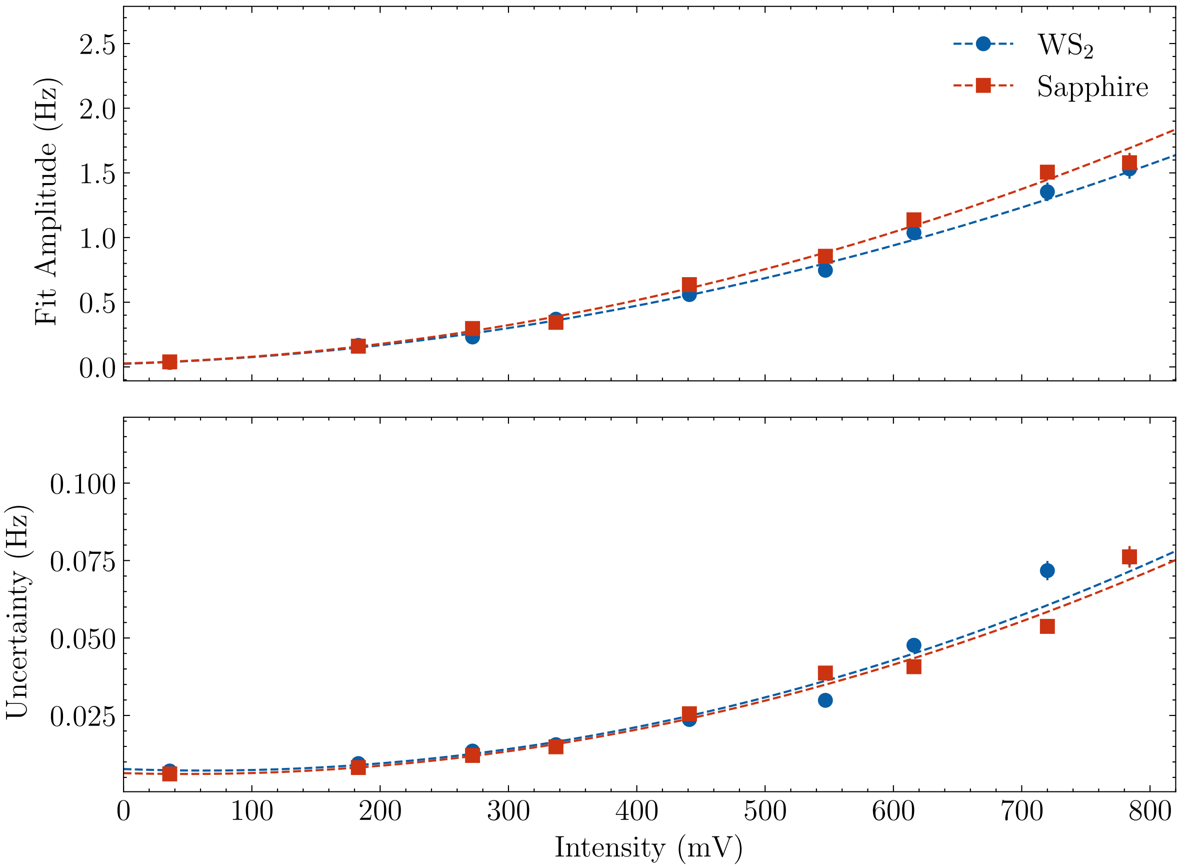

Figure 4.3: AFM autocorrelation amplitude and noise as a function of intensity over WS$_2$ and sapphire. All data sets were fitted with a second-order polynomial.

The CPD was compensated at the two locations in which the intensity measurements were conducted to get as close to the same tip-sample separation as possible. All other parameters, such as the frequency shift setpoint, remained the same.

The intensity measurements shown in figure 4.3 are very similar on both the sapphire substrate as well as the WS$_2$ flake. Both of the measurements were fitted with a second-order polynomial of the form $Ax^2 + Bx + C$, and the A parameter is proportional to $\chi^{(2)}$. The fitted A values for the intensity measurements were found to be

$$A^{\mathrm{WS_2}}_{\mathrm{Amplitude}} = 2.0 \pm 0.2, \tag{4.5}$$

$$A^{\mathrm{Sapphire}}_{\mathrm{Amplitude}} = 2.3 \pm 0.2, \tag{4.6}$$

$$A^{\mathrm{WS_2}}_{\mathrm{Noise}} = 1.3 \pm 0.2, \tag{4.7}$$

$$A^{\mathrm{Sapphire}}_{\mathrm{Noise}} = 1.2 \pm 0.2. \tag{4.8}$$

The units in these parameters are not important, as only the relative comparisons between the A values for the different materials are what signify the relative differences in $\chi^{(2)}$. Clearly, there is very little difference in $\chi^{(2)}$ between the two locations on the sample as the values of A in the two measurements overlap with each other in error. This will be further verified by the spatial measurement in the next section, and a possible explanation will be discussed.

4.1.3 Spatial Measurement

Here, a spatial measurement was conducted at a constant intensity, and is shown in figure 4.4. The spatial measurement was conducted in a straight line that began on the sapphire substrate and moved onto the WS_2 flake in 20 nm steps. At each step, the CPD was compensated to ensure constant tip-sample separation. While the z and CPD values changed from one material to the other in a way that was consistent with the KPFM scan shown in figure 4.1, there was very little contrast in the autocorrelation amplitude and noise measurements. This is consistent with what was shown in the intensity measurements in the previous section.

While it is expected for any surface to have a nonzero $\chi^{(2)}$, it would be surprising for a clean sapphire surface to have a $\chi^{(2)}$ that is comparable to the massive $\chi^{(2)}$ of WS_2. Sapphire is not typically used for second-order optical processes, and even materials that are typically used, like BBO, only have $\chi^{(2)}$ on the order of 1 pm/V [23], much smaller than reported values on the order of 1 nm/V for monolayer WS_2 [37, 38]. A possible explanation for why the nonlinear measurements on the sapphire substrate used here are comparable to that of the WS_2 flakes is that it is not a completely clean sapphire surface. Indeed, one can see that the topography of the sapphire substrate in figures 4.1a, c is very rough, and may contain significant amounts of the precursors used in the CVD process that did not aggregate into larger flakes. It is possible that these precursors are contributing to the nonlinear signal measured by AFM.

Despite the lack of contrast between the sapphire and the WS_2 in the nonlinear measurements, the measurements discussed in this chapter have shown a clear correlation between the autocorrelation and noise measurements. To show a better contrast between the flake and the substrate, the measurements should be done on exfoliated flakes on a less responsive substrate such as SiO_2.

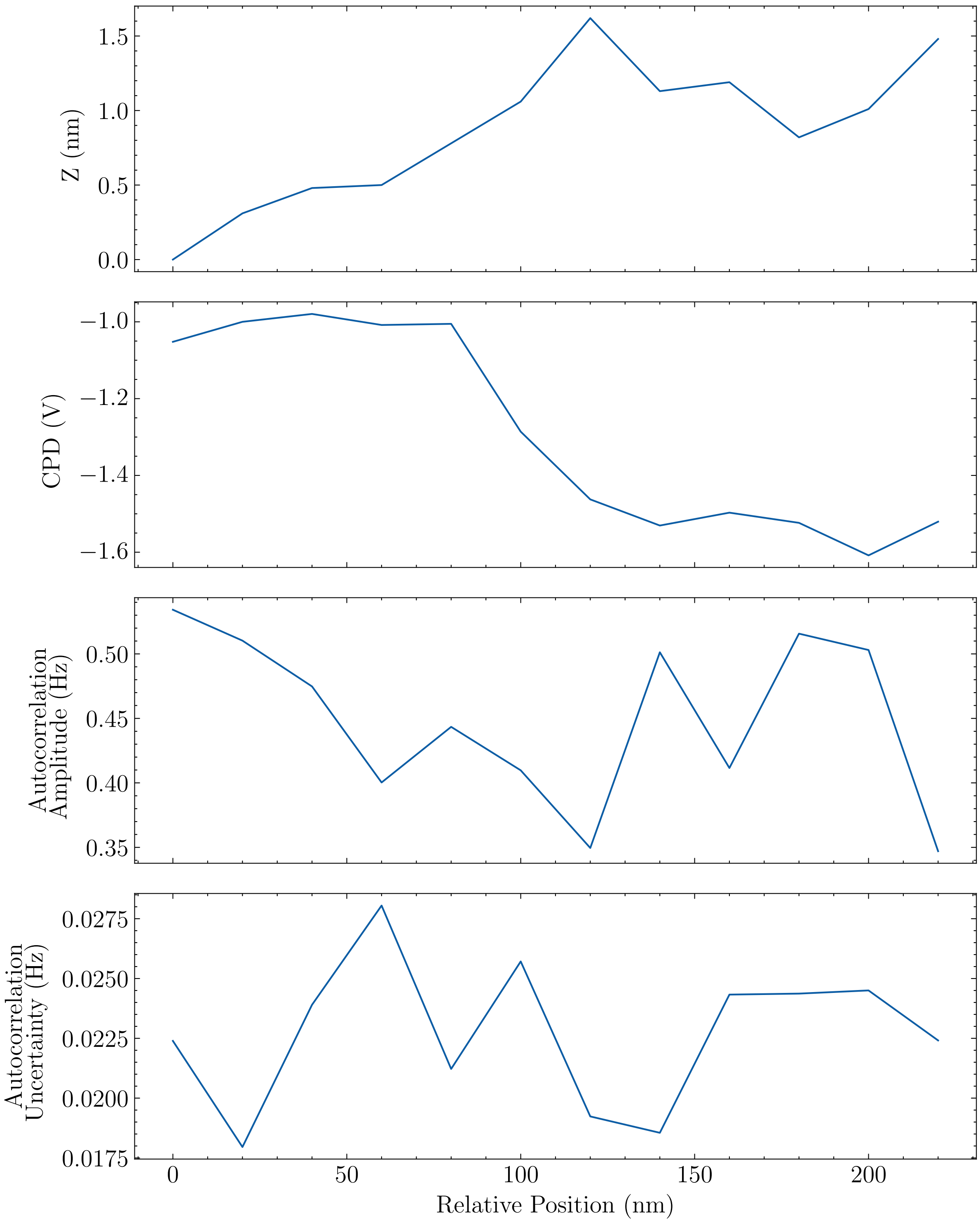

Figure 4.4: A line measurement conducted over the sapphire (0-100 nm) and WS_2 flake (100-220 nm).

Chapter 5

Conclusion and Outlook

This work has demonstrated the correlation between autocorrelation amplitude and noise measurements of $\chi^{(2)}$. This correlation has been demonstrated with laser intensity and also AFM tip distance measurements on merocyanine dye HB238 and on CVD grown WS_2 on sapphire. A spatial measurement was attempted on the WS_2 sample, but there was very little contrast between the measurements on the flake and on the substrate. A WS_2 flake, or any TMD flake, on a SiO_2 substrate would likely be a better candidate, as SiO_2 has a very small nonlinear response and the signal from the TMD flake should dominate.

Despite an inconclusive result in the spatial measurement that has been shown in this work, the correlation between the autocorrelation amplitude and noise shows a very promising development in nonlinear optical measurements with ultrafast AFM that will allow for much finer spatial characterization of $\chi^{(2)}$ in less time. One interesting study in which this could be applied in is in understanding how defect structure affects $\chi^{(2)}$. This could be applied to both manufactured defects as well as intrinsic defects that are already present in the material. There have been numerous studies with AFM that have shown how one can characterize the structure of defects, such as that of SiO_2 as well as $MoSe_2$[47, 48]. The location of defects can be conducted with AFM dissipation scans, which maps out the driving energy of the cantilever. In such scans, the tip is brought close to the surface to induce band bending. When the tip comes close to a defect, the bands will align with the energy levels of the defect and allow for tunneling of electrons between the defect and the bulk material, resulting in energy losses in the cantilever and showing up as a bright spot in the dissipation scan. A raster scan of the dissipation will show bright rings centered around defects in the material. An example of such a dissipation scan is shown in figure 5.1, which was done over SiO_2. The rings in figure 5.1 correspond to the locations of defects in the interface between the bulk Si and the oxide overgrowth, and the size of the rings correspond to the energy levels of the defects [47]. An ultrafast AFM noise measurement conducted over a region with defects can show the correlation between the defect structure and their local $\chi^{(2)}$. Once this correlation is understood, it would be interesting to develop materials with a high density of defects with large $\chi^{(2)}$ that could be made into devices that emit entangled photon pairs through half harmonic generation. Such photon pair emitters would be very useful in quantum applications. Such correlation of $\chi^{(2)}$ to defect structure could also be important in minimizing optically active defects that are detrimental to a device, as was demonstrated on the SiC/SiO_2 interface [49]. The precise understanding of defects in TMD materials has been shown to be an important topic of study [50, 51].

There are still unanswered questions about measuring nonlinear optical effects with ultrafast AFM. For example, how much of the material does ultrafast AFM probe? If the material of interest is deposited on a substrate (like glass in the HB238 sample, or sapphire in the WS_2 sample), how much does the sample-substrate interface contribute to the nonlinear response of the AFM? After all, the interface does have a non-centrosymmetric crystal structure and thus has a nonzero contribution to the nonlinear response. One way these questions could be answered is by studying HB238 thin film samples of various thicknesses with ultrafast AFM. This will show how the signal (and noise) vary as a function of sample thickness, and provide insight into how deep the ultrafast AFM technique probes the sample, and how the sample-substrate interface contributes to the nonlinear response of the AFM.

Further characterizations of the noise measurement of $\chi^{(2)}$ should be done. In particular,

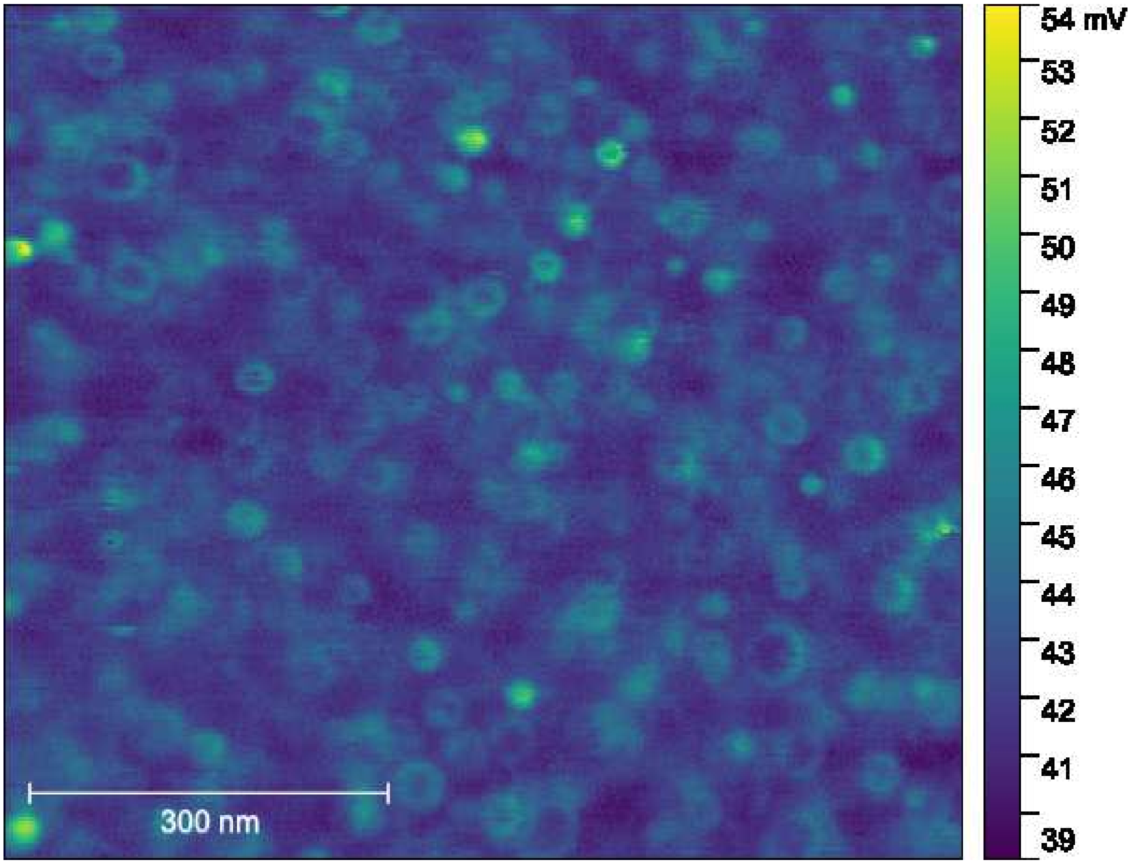

Figure 5.1: Dissipation scan of a SiO_2 surface with a 3 nm oxide overgrowth. The light blue rings indicate the locations of defects in the Si/SiO_2 interface, and their radii correspond to the energy levels of the defects.

what kind of noise is being measured and how does it depend on the sampling rate of the signal? Understanding the colour of the noise will provide insight into the mechanics that generate the noise.

Bibliography

[1] J. Czochralski, *Ein neues Verfahren zur Messung der Kristallisationsgeschwindigkeit der Metalle*, Zeitschrift für Physikalische Chemie **92**, 219–221 (1918).

[2] M. Knoll and E. Ruska, *Beitrag zur geometrischen Elektronenoptik. I*, Annalen der Physik **404**, 607–640 (1932), `https://onlinelibrary.wiley.com/doi/pdf/10.1002/andp.19324040506`.

[3] M. Knoll and E. Ruska, *Das Elektronenmikroskop*, Zeitschrift für Physik **78**, 318–339 (1932).

[4] G. Binnig and H. Rohrer, *Scanning tunneling microscopy*, Surface Science **126**, 236–244 (1983).

[5] F. Hund, *Zur Deutung der Molekelspektren. I*, Zeitschrift für Physik **40**, 742–764 (1927).

[6] J. Curie and P. Curie, *Contractions et dilatations produites par des tensions dans les cristaux hémièdres à faces inclinées*, Comptes Rendus **93**, 1137–1140 (1881).

[7] B. Voigtländer, *Scanning Probe Microscopy: Atomic Force Microscopy and Scanning Tunneling Microscopy*, Springer Berlin Heidelberg (2015).

[8] R. Young, J. Ward, and F. Scire, *The Topografiner: An Instrument for Measuring Surface Microtopography*, Review of Scientific Instruments **43**, 999–1011 (1972), `https://doi.org/10.1063/1.1685846`.

[9] G. Binnig, C. F. Quate, and C. Gerber, *Atomic Force Microscope*, Phys. Rev. Lett. **56**, 930–933 (1986).

[10] F. J. Giessibl, *Advances in atomic force microscopy*, Rev. Mod. Phys. **75**, 949–983 (2003).

[11] Y. Martin, C. C. Williams, and H. K. Wickramasinghe, *Atomic force microscope–force mapping and profiling on a sub 100-Å scale*, Journal of Applied Physics **61**, 4723–4729 (1987), `https://pubs.aip.org/aip/jap/article-pdf/61/10/4723/7994030/4723_1_online.pdf`.

[12] T. R. Albrecht, P. Grütter, D. Horne, and D. Rugar, *Frequency modulation detection using high-Q cantilevers for enhanced force microscope sensitivity*, Journal of Applied Physics **69**, 668–673 (1991), `https://doi.org/10.1063/1.347347`.

[13] N. P. Outreach, *The Nobel Prize in Chemistry 1999.*

[14] A. H. Zewail, *Femtochemistry: Atomic-Scale Dynamics of the Chemical Bond*, The Journal of Physical Chemistry A **104**, 5660–5694 (2000).

[15] R. J. Hamers and D. G. Cahill, *Ultrafast time resolution in scanned probe microscopies*, Applied Physics Letters **57**, 2031–2033 (1990), `https://pubs.aip.org/aip/apl/article-pdf/57/19/2031/18479189/2031_1_online.pdf`.

[16] T. L. Cocker, V. Jelic, M. Gupta, S. J. Molesky, J. A. J. Burgess, G. D. L. Reyes, L. V. Titova, Y. Y. Tsui, M. R. Freeman, and F. A. Hegmann, *An ultrafast terahertz scanning tunnelling microscope*, Nature Photonics **7**, 620–625 (2013).

[17] Y. Terada, S. Yoshida, O. Takeuchi, and H. Shigekawa, *Real-space imaging of transient carrier dynamics by nanoscale pump–probe microscopy*, Nature Photonics **4**, 869–874 (2010).

[18] J. Jahng, J. Brocious, D. A. Fishman, S. Yampolsky, D. Nowak, F. Huang, V. A. Apkarian, H. K. Wickramasinghe, and E. O. Potma, *Ultrafast pump-probe force microscopy with nanoscale resolution*, Applied Physics Letters **106**, 083113 (2015), `https://pubs.aip.org/aip/apl/article-pdf/doi/10.1063/1.4913853/13593727/083113_1_online.pdf`.

[19] Z. Schumacher, A. Spielhofer, Y. Miyahara, and P. Grutter, *The limit of time resolution in frequency modulation atomic force microscopy by a pump-probe approach*, Applied Physics Letters **110**, 053111 (2017), `https://pubs.aip.org/aip/apl/article-pdf/doi/10.1063/1.4975629/14493749/053111_1_online.pdf`.

[20] Z. Schumacher, Y. Miyahara, A. Spielhofer, and P. Grutter, *Measurement of Surface Photovoltage by Atomic Force Microscopy under Pulsed Illumination*, Phys. Rev. Applied **5**, 044018 (2016).

[21] I. Rajapaksa, K. Uenal, and H. K. Wickramasinghe, *Image force microscopy of molecular resonance: A microscope principle*, Applied Physics Letters **97**, 073121 (2010), `https://pubs.aip.org/aip/apl/article-pdf/doi/10.1063/1.3480608/14436966/073121_1_online.pdf`.

[22] T. Santiago-Cruz, A. Fedotova, V. Sultanov, M. A. Weissflog, D. Arslan, M. Younesi, T. Pertsch, I. Staude, F. Setzpfandt, and M. Chekhova, *Photon Pairs from Resonant Metasurfaces*, Nano Letters **21**, 4423–4429 (2021).

[23] R. Boyd, *Nonlinear Optics*, Elsevier Science (2020).

[24] V. Giovannetti, S. Lloyd, and L. Maccone, *Quantum-Enhanced Measurements: Beating the Standard Quantum Limit*, Science **306**, 1330–1336 (2004), `https://www.science.org/doi/pdf/10.1126/science.1104149`.

[25] Z. Schumacher, R. Rejali, R. Pachlatko, A. Spielhofer, P. Nagler, Y. Miyahara, D. G. Cooke, and P. Grütter, *Nanoscale force sensing of an ultrafast nonlinear optical re-*

sponse, Proceedings of the National Academy of Sciences **117**, 19773–19779 (2020), `https://www.pnas.org/doi/pdf/10.1073/pnas.2003945117`.

[26] J. Spiegelberg, *Measuring the nonlinear optical properties of monolayer Tungsten disulfide with optically-pumped atomic force microscopy* (2022).

[27] H. Hölscher, U. Schwarz, and R. Wiesendanger, *Calculation of the frequency shift in dynamic force microscopy*, Applied Surface Science **140**, 344–351 (1999).

[28] D. Griffiths, *Introduction to Electrodynamics*, v. 2, Cambridge University Press (2017).

[29] A. Owyoung, *The Origins of the Nonlinear Refractive Indices of Liquids and Glasses*, Phd dissertation, California Institute of Technology (1971).

[30] P. D. Maker, R. W. Terhune, M. Nisenoff, and C. M. Savage, *Effects of Dispersion and Focusing on the Production of Optical Harmonics*, Phys. Rev. Lett. **8**, 21–22 (1962).

[31] S. Hooker and C. Webb, *Laser Physics*, Oxford Master Series in Physics, OUP Oxford (2010).

[32] A. Liscio, V. Palermo, D. Gentilini, F. Nolde, K. Müllen, and P. Samorì, *Quantitative Measurement of the Local Surface Potential of π-Conjugated Nanostructures: A Kelvin Probe Force Microscopy Study*, Advanced Functional Materials **16**, 1407–1416 (2006), `https://onlinelibrary.wiley.com/doi/pdf/10.1002/adfm.200600145`.

[33] S. A. Burke, J. M. LeDue, Y. Miyahara, J. M. Topple, S. Fostner, and P. Grütter, *Determination of the local contact potential difference of PTCDA on NaCl: a comparison of techniques*, Nanotechnology **20**, 264012 (2009).

[34] H. Bürckstümmer, E. V. Tulyakova, M. Deppisch, M. R. Lenze, N. M. Kronenberg, M. Gsänger, M. Stolte, K. Meerholz, and F. Würthner, *Efficient Solution-Processed*

Bulk Heterojunction Solar Cells by Antiparallel Supramolecular Arrangement of Dipolar Donor–Acceptor Dyes, Angewandte Chemie International Edition **50**, 11628–11632 (2011), `https://onlinelibrary.wiley.com/doi/pdf/10.1002/anie.201105133`.

[35] N. Gildemeister, G. Ricci, L. Böhner, J. M. Neudörfl, D. Hertel, F. Würthner, F. Negri, K. Meerholz, and D. Fazzi, *Understanding the structural and charge transport property relationships for a variety of merocyanine single-crystals: a bottom up computational investigation*, J. Mater. Chem. C **9**, 10851–10864 (2021).

[36] R. Schäfer, L. Böhner, M. Schiek, D. Hertel, K. Meerholz, and K. Lindfors, *Strong Light–Matter Interaction of Molecular Aggregates with Two Excitonic Transitions*, ACS Photonics **11**, 111–120 (2024).

[37] C. Janisch, Y. Wang, D. Ma, N. Mehta, A. L. Elías, N. Perea-López, M. Terrones, V. Crespi, and Z. Liu, *Extraordinary Second Harmonic Generation in Tungsten Disulfide Monolayers*, Scientific Reports **4**, 5530 (2014).

[38] X. Fan, Y. Jiang, X. Zhuang, H. Liu, T. Xu, W. Zheng, P. Fan, H. Li, X. Wu, X. Zhu, Q. Zhang, H. Zhou, W. Hu, X. Wang, L. Sun, X. Duan, and A. Pan, *Broken Symmetry Induced Strong Nonlinear Optical Effects in Spiral WS2 Nanosheets*, ACS Nano **11**, 4892–4898 (2017).

[39] L. Zehnder, *Ein neuer Interferenzrefraktor*, Zeitschrift für Instrumentenkunde **11**, 275–285 (1891).

[40] L. Mach, *Ueber einen Interferenzrefraktor*, Zeitschrift für Instrumentenkunde **12**, 89–93 (1892).

[41] D. N. Nikogosyan, *Beta barium borate (BBO)*, Applied Physics A **52**, 359–368 (1991).

[42] A. A. Milner, K. Zhang, V. Garmider, and Y. Prior, *Heating of an Atomic Force Microscope tip by femtosecond laser pulses*, Applied Physics A **99**, 1–8 (2010).

[43] C. J. Chen, *Introduction to Scanning Tunneling Microscopy*, Oxford University Press (2007).

[44] G. Yi, H. Lee, J. Jiannan, B. J. Chun, S. Han, H. Kim, Y. W. Kim, D. Kim, S.-W. Kim, and Y.-J. Kim, *Nonlinear third harmonic generation at crystalline sapphires*, Opt. Express **25**, 26002–26010 (2017).

[45] H. R. Gutiérrez, N. Perea-López, A. L. Elías, A. Berkdemir, B. Wang, R. Lv, F. López-Urías, V. H. Crespi, H. Terrones, and M. Terrones, *Extraordinary Room-Temperature Photoluminescence in Triangular WS2 Monolayers*, Nano Letters **13**, 3447–3454 (2013).

[46] S. Hudlet, M. Saint Jean, C. Guthmann, and J. Berger, *Evaluation of the capacitive force between an atomic force microscopy tip and a metallic surface*, The European Physical Journal B - Condensed Matter and Complex Systems **2**, 5–10 (1998).

[47] M. Cowie, T. J. Z. Stock, P. C. Constantinou, N. J. Curson, and P. Grütter, *Spatially Resolved Dielectric Loss at the* Si/SiO_2 *Interface*, Phys. Rev. Lett. **132**, 256202 (2024).

[48] M. Cowie, R. Plougmann, Z. Schumacher, and P. Grütter, *Single-dopant band bending fluctuations in* $MoSe_2$ *measured with electrostatic force microscopy*, Phys. Rev. Mater. **6**, 104002 (2022).

[49] B. Johnson, J. Woerle, D. Haasmann, C.-K. Lew, R. Parker, H. Knowles, B. Pingault, M. Atature, A. Gali, S. Dimitrijev, M. Camarda, and J. McCallum, *Optically Active Defects at the* SiC/SiO_2 *Interface*, Phys. Rev. Appl. **12**, 044024 (2019).

[50] J. A. Robinson and B. Schuler, *Engineering and probing atomic quantum defects in 2D semiconductors: A perspective*, Applied Physics Letters **119**, 140501 (2021), `https://doi.org/10.1063/5.0065185`.

[51] J. Jiang, T. Xu, J. Lu, L. Sun, and Z. Ni, *Defect Engineering in 2D Materials: Precise Manipulation and Improved Functionalities*, Research **2019** (2019), `https://spj.science.org/doi/pdf/10.34133/2019/4641739`.